Torabi, Jalal; Niiranen, Jarkko; Ansari, Reza

Multi-patch variational differential quadrature method for shear-deformable strain gradient plates

Published in:
International Journal for Numerical Methods in Engineering

DOI:
10.1002/nme.6939

Published: 30/05/2022

Received: 9 November 2021 | Revised: 18 January 2022 | Accepted: 7 February 2022

DOI: 10.1002/nme.6939

RESEARCH ARTICLE

WILEY

Multi-patch variational differential quadrature method for shear-deformable strain gradient plates

Jalal Torabi[1] | **Jarkko Niiranen**[1] | **Reza Ansari**[2]

[1]Department of Civil Engineering, School of Engineering, Aalto University, Aalto, Finland

[2]Faculty of Mechanical Engineering, University of Guilan, Rasht, Iran

Correspondence
Jalal Torabi, Department of Civil Engineering, School of Engineering, Aalto University, P.O. Box 12100, Aalto 00076, Finland.
Email: jalal.torabi@aalto.fi

Abstract

The integration of generalized differential quadrature techniques and finite element (FE) methods has been developed during the past decade for engineering problems within classical continuum theories. Hence, the main objective of the present study is to propose a novel numerical strategy called the multi-patch variational differential quadrature (VDQ) method to model the structural behavior of plate structures obeying the shear deformation plate theory within the strain gradient elasticity theory. The idea is to divide the two-dimensional solution domain of the plate model into sub-domains, called patches, and then to apply the VDQ method along with the FE mapping technique for each patch. The formulation is presented in a weak form and due to the C^1-continuity requirements the corresponding compatibility conditions are applied through the patch interfaces. The Lagrange multiplier technique and the penalty method are implemented to apply the higher-order compatibility conditions and boundary conditions, respectively. To show the efficiency of the proposed method, numerical results are provided for plate structures with both regular and irregular solution domains. The provided numerical examples demonstrate the applicability and accuracy of the method in predicting the bending and vibration behavior of plate structures following the higher-order plate model.

KEYWORDS

bending analysis, first-order shear deformation plate theory, multi-patch technique, strain gradient elasticity, variational differential quadrature, vibration analysis

1 | INTRODUCTION

The governing equations of the mathematical models for most engineering problems can be presented with either the weak form variational formulations by defining a proper energy functional or the set of partial differential equations (PDEs) and related boundary conditions. The solutions of these governing equations play an important role in the advancements of engineering applications. Due to the demands regarding technological improvements, several numerical discretization methods such as finite element (FE), meshless, finite difference, and differential quadrature (DQ) methods have been developed during the past decades to provide methodical numerical solution strategies for complex engineering problems. Each of these numerical approaches has its advantages and disadvantages. For instance, although low-order FE or meshless methods can be used in a diverse range of advanced engineering problems, a large number of degrees of freedom (DOF) should be employed to find accurate results at specific points. In comparison, higher-order methods such as the DQ method could yield precise solutions with a lower number of grid points, but the application range might be limited to regular or structured solution domains. During the last decade, some effort has been made to overcome this drawback. Shu[1] introduced the generalized differential quadrature (GDQ) method in which the derivatives of the unknown function are approximated as a weighted sum of function values at certain grid points. Due to the high accuracy and straightforward implementation, the performance of the GDQ method in several mechanical engineering applications has been demonstrated.[2–8] Even though the GDQ method was originally developed for the strong form of the governing equations (i.e., the PDEs of motion), Ansari and his co-authors extended the implementation of the GDQ discretization approach to the weak form variational formulations, and the method was, accordingly, called the variational differential quadrature (VDQ) method.[9] It should be noticed that the VDQ method can be directly applied to any energy functional, one does not need to analytically derive the strong form of the governing equations. Some applications of the VDQ method have been demonstrated in References 10–13.

It is well known that in its original form (both strong and weak form implementations), the GDQ method has its limitations in the presence of problems with complex solution domains. In the case of irregular convex domains, a mapping technique was proposed to enhance the applications of the approach.[14–18] The first attempts for extending the GDQ method to irregular domains can be found in Reference 19. Besides, Tornabene and his colleagues integrated the accuracy of the GDQ method with the element-wise idea of the FE method to propose the generalized differential quadrature finite element method (GDQFEM) to improve the applicability of the GDQ technique in more complex problems.[20] The efficiency of the GDQFEM has been recently demonstrated in many problems of solid mechanics within the classical continuum assumptions.[21–23] It is worth noting that GDQFEM relies on the strong form of the problem, and it can be applied for nonconvex solution domains. Furthermore, the idea of the VDQ method has recently been broadened for irregular domains by introducing the variational differential quadrature element method (VDQFEM) in which the domain is first divided into sub-domains (or elements) and the VDQ approach is applied within each element.[24–26] It should be pointed out that in the case of GDQFEM, the physical domain is divided into some distinct patches (or elements) and, unlike in the FE method, no shared nodes are considered between the patches but the compatibility conditions are directly enforced for the edges of the patches to meet the continuity requirements between the elements.[20] However, in the case of VDQFEM the basic idea of the FE element is employed and instead of common shape functions, the VDQ discretization approach is applied within each element.[24]

Aside the classical continuum mechanics, the strain gradient (SG) elasticity theory,[27,28] as one of the unified generalized continuum theories, presents a coherent theoretical framework in which strain gradients and the corresponding material length scale parameters provide an efficient formulation to model the mechanical behavior of small-scale[29–33] or lattice[34–38] structures. The presence of the strain gradient terms makes the formulation more complicated and therefore alternative numerical strategies should be employed to provide accurate solutions. Different numerical approaches such as higher-order FE methods[39–43] and isogeometric analysis (IGA)[44–48] have been recently developed to overcome this problem. Deriving higher-order FEs that satisfy the C^1-continuity conditions, for instance, are always complicated particularly for unstructured meshing. The applications of elements with Lagrange multipliers or penalty formulations also make the theoretical formulation more complex since the derivation of governing equations in a mixed-formulation might be needed. Furthermore, IGA can be straightforwardly utilized for problems with convex domains, whereas in the case of more complex domains multi-patch approaches should be implemented.[49] It is worth noting that the basic version of VDQFEM cannot be applied as such to strain gradient problems since the higher-order continuity requirements cannot be guaranteed at the edges between elements. Therefore, developing an alternative numerical solution technique can significantly contribute to the topical area and provide a useful approach for further studies. To address these challenges, the main purpose of the present study is to develop a novel numerical strategy, called the multi-patch VDQ method, for SG shear deformation plate problems with complex domains. As the governing equations for the SG shear deformation plate model itself can be found in the open literature and the fundamentals of the VDQ technique for classical continuum plate problems have already been studied, the main novelties of the present study are the following: first, the VDQ discretization and accuracy analysis for the SG first-order shear deformation plate formulation; second, the implementation and accuracy analysis of the multi-patch VDQ technique for higher-order compatibility conditions at the interface edges of the patches. In this regard, the physical domain is divided into several patches, and then by employing the advantages of the VDQ method and a FE mapping technique the energy functional of the problem is discretized within each distinct patch, with no shared nodes between the patches. Since the SG shear deformation plate problem is formulated as a variational formulation, second-order derivatives of the displacement components are involved in the energy functional. Hence, to meet the required C^1-continuity conditions at the interfaces of the patches, the compatibility conditions for the function values of the displacement components, their first-order derivatives, and their mixed second-order derivatives are applied by using the Lagrange multiplier technique.

The rest of the manuscript is organized as follows. The energy functional for the SG shear deformation plate problem is derived in Section 2. The discretization method based on the VDQ method and a FE mapping technique is developed for each patch in Section 3. The details of the multi-patch approach, along with the implementation of the compatibility conditions, is provided in Section 3.3. A wide range of numerical results is presented in Section 4, to demonstrate the applicability and accuracy of the proposed numerical solution strategy. Finally, Section 5 gives some conclusions on the study.

2 | GOVERNING EQUATIONS

2.1 | Strain gradient theory

As one of the unified generalized continuum theories, the SG elasticity theory proposes a flexible theoretical formulation for structural mechanics of small-scale solids or microarchitectural mechanical metamaterials. On the basis of isotropic SG elasticity, the strain energy functional is expressed in terms of strains (ε_{pq}) and strain gradients (η_{pqr}) along with the corresponding classical and higher-order material parameters:

$$\widetilde{\mathfrak{U}} = \frac{1}{2}\lambda\varepsilon_{pp}\varepsilon_{qq} + \mu\varepsilon_{pq}\varepsilon_{pq} + \alpha_1\eta_{rpp}\eta_{qqr} + \alpha_2\eta_{qqp}\eta_{rrp} + \alpha_3\eta_{rpp}\eta_{rqq} + \alpha_4\eta_{pqr}\eta_{pqr} + \alpha_5\eta_{pqr}\eta_{rqp} \tag{1}$$

in which, according to the assumption of linear kinematics, strains and strain gradients are given as

$$\begin{aligned} \varepsilon_{pq} &= \frac{1}{2}\left(u_{p,q} + u_{q,p}\right) = \varepsilon_{qp} \\ \eta_{pqr} &= \frac{1}{2}\left(u_{p,q} + u_{q,p}\right)_{,r} = \eta_{qpr} \end{aligned} \tag{2}$$

where u_p are the displacements, λ and μ are the classical Lame's constants and α_i $(i = 1, 2, \ldots, 5)$ denote higher-order SG material parameters. By taking the strain energy into account, the classical and generalized constitutive equations for stresses and double stresses are defined as

$$\begin{aligned} \sigma_{pq} &= \frac{1}{2}\left(\frac{\partial\widetilde{\mathfrak{U}}}{\partial\varepsilon_{pq}} + \frac{\partial\widetilde{\mathfrak{U}}}{\partial\varepsilon_{qp}}\right) = \lambda\varepsilon_{mm}\delta_{pq} + 2\mu\varepsilon_{pq} \\ \Sigma_{pqr} &= \frac{1}{2}\left(\frac{\partial\widetilde{\mathfrak{U}}}{\partial\eta_{pqr}} + \frac{\partial\widetilde{\mathfrak{U}}}{\partial\eta_{qpr}}\right) \\ &= \tfrac{1}{2}\alpha_1\left(\eta_{mmp}\delta_{qr} + \eta_{rmm}\delta_{pq} + \eta_{mmq}\delta_{pr}\right) + 2\alpha_2\eta_{mmr}\delta_{pq} \\ &\quad + \alpha_3\left(\eta_{pmm}\delta_{qr} + \eta_{qmm}\delta_{pr}\right) + 2\alpha_4\eta_{pqr} + \alpha_5\left(\eta_{rqp} + \eta_{rpq}\right) \end{aligned}$$

More details on the fundamentals of SG elasticity can be found in References 27, 30, 32, 38, for instance. In what follows, the formulation of SG elasticity for the shear deformation plate theory (SDPT) is given.

2.2 | Shear deformation plate model

In what follows, a Cartesian coordinate system (X, Y, Z) is used to formulate the governing equations of the SG plate problem. By following the SDPT and by setting U_0, V_0, W_0 for mid-surface displacements and Ψ, Φ for rotations, the vector of the displacement field $\mathbf{q} = [U(X,Y,Z)\ V(X,Y,Z)\ W(X,Y,Z)]^{\mathrm{T}}$ can be represented by

$$\boldsymbol{q} = \boldsymbol{\mathcal{A}}_0\boldsymbol{q}_0, \quad \mathcal{A}_0 = \begin{bmatrix} 1 & 0 & 0 & Z & 0 \\ 0 & 1 & 0 & 0 & Z \\ 0 & 0 & 1 & 0 & 0 \end{bmatrix}, \quad \boldsymbol{q}_0 = \begin{bmatrix} U_0(X,Y) \\ V_0(X,Y) \\ W_0(X,Y) \\ \Psi(X,Y) \\ \Phi(X,Y) \end{bmatrix}. \tag{4}$$

Under the standard geometrically linear kinematic assumptions, the strain vector is

$$\boldsymbol{\varepsilon} = \begin{bmatrix} \varepsilon_{XX} \\ \varepsilon_{YY} \\ \varepsilon_{XY} \\ \gamma_{XZ} \\ \gamma_{YZ} \end{bmatrix} = \boldsymbol{\mathcal{A}}_c\boldsymbol{E}_c\boldsymbol{q}_0, \tag{5}$$

with

$$\boldsymbol{\mathcal{A}}_c = \begin{bmatrix} 1 & 0 & 0 & Z & 0 & 0 & 0 & 0 \\ 0 & 1 & 0 & 0 & Z & 0 & 0 & 0 \\ 0 & 0 & 1 & 0 & 0 & Z & 0 & 0 \\ 0 & 0 & 0 & 0 & 0 & 0 & 1 & 0 \\ 0 & 0 & 0 & 0 & 0 & 0 & 0 & 1 \end{bmatrix}, \boldsymbol{E}_c = \begin{bmatrix} \partial_X & 0 & 0 & 0 & 0 \\ 0 & \partial_Y & 0 & 0 & 0 \\ \partial_Y & \partial_X & 0 & 0 & 0 \\ 0 & 0 & 0 & \partial_X & 0 \\ 0 & 0 & 0 & 0 & \partial_Y \\ 0 & 0 & 0 & \partial_Y & \partial_X \\ 0 & 0 & \partial_X & 1 & 0 \\ 0 & 0 & \partial_Y & 0 & 1 \end{bmatrix}, \tag{6}$$

where $\mathbf{E}_c$ denotes the linear matrix operator related to the strain vector. By following Equation (2), the strain gradient vector is presented as

$$\boldsymbol{\eta} = \begin{bmatrix} \boldsymbol{\eta}_1 \\ \boldsymbol{\eta}_2 \\ \boldsymbol{\eta}_3 \\ \boldsymbol{\eta}_4 \end{bmatrix} = \boldsymbol{\mathcal{A}}_s\boldsymbol{E}_s\boldsymbol{q}_0, \tag{7}$$

with the components

$$\boldsymbol{\eta}_1 = \begin{bmatrix} \varepsilon_{XX,X} \\ \varepsilon_{YY,X} \\ \gamma_{YX,Y} \end{bmatrix} = \boldsymbol{\mathcal{A}}_s^1\boldsymbol{E}_s^1\boldsymbol{q}_0, \boldsymbol{\eta}_2 = \begin{bmatrix} \varepsilon_{YY,Y} \\ \varepsilon_{XX,Y} \\ \gamma_{XY,X} \end{bmatrix} = \boldsymbol{\mathcal{A}}_s^2\boldsymbol{E}_s^2\boldsymbol{q}_0, \boldsymbol{\eta}_3 = \begin{bmatrix} \varepsilon_{XX,Z} \\ \gamma_{XZ,X} \\ \varepsilon_{YY,Z} \\ \gamma_{YZ,Y} \end{bmatrix} = \boldsymbol{\mathcal{A}}_s^3\boldsymbol{E}_s^3\boldsymbol{q}_0, \boldsymbol{\eta}_4 = \begin{bmatrix} \gamma_{XY,Z} \\ \gamma_{YZ,X} \\ \gamma_{ZX,Y} \end{bmatrix} = \boldsymbol{\mathcal{A}}_s^4\boldsymbol{E}_s^4\boldsymbol{q}_0 \tag{8}$$

where

$$\boldsymbol{\mathcal{A}}_s^1 = \boldsymbol{\mathcal{A}}_s^2 = \begin{bmatrix} 1 & 0 & 0 & Z & 0 & 0 \\ 0 & 1 & 0 & 0 & Z & 0 \\ 0 & 0 & 1 & 0 & 0 & Z \end{bmatrix}, \boldsymbol{\mathcal{A}}_s^3 = \begin{bmatrix} 1 & 0 & 0 & 0 \\ 0 & 1 & 0 & 0 \\ 0 & 0 & 1 & 0 \\ 0 & 0 & 0 & 1 \end{bmatrix}, \boldsymbol{\mathcal{A}}_s^4 = \begin{bmatrix} 1 & 0 & 0 \\ 0 & 1 & 0 \\ 0 & 0 & 1 \end{bmatrix} \tag{9}$$

and the strain gradient matrix operators $\mathbf{E}_s^j, j = 1, 2, 3, 4$, are defined as

$$\boldsymbol{E}_s^1 = \begin{bmatrix} \partial_{XX} & 0 & 0 & 0 & 0 \\ 0 & \partial_{XY} & 0 & 0 & 0 \\ \partial_{YY} & \partial_{XY} & 0 & 0 & 0 \\ 0 & 0 & 0 & \partial_{XX} & 0 \\ 0 & 0 & 0 & 0 & \partial_{XY} \\ 0 & 0 & 0 & \partial_{YY} & \partial_{XY} \end{bmatrix}, \boldsymbol{E}_s^2 = \begin{bmatrix} 0 & \partial_{YY} & 0 & 0 & 0 \\ \partial_{XY} & 0 & 0 & 0 & 0 \\ \partial_{XY} & \partial_{XX} & 0 & 0 & 0 \\ 0 & 0 & 0 & 0 & \partial_{YY} \\ 0 & 0 & 0 & \partial_{XY} & 0 \\ 0 & 0 & 0 & \partial_{XY} & \partial_{XX} \end{bmatrix},$$
$$\boldsymbol{E}_s^3 = \begin{bmatrix} 0 & 0 & 0 & \partial_X & 0 \\ 0 & 0 & \partial_{XX} & \partial_X & 0 \\ 0 & 0 & 0 & 0 & \partial_Y \\ 0 & 0 & \partial_{YY} & 0 & \partial_Y \end{bmatrix}, \quad \boldsymbol{E}_s^4 = \begin{bmatrix} 0 & 0 & 0 & \partial_Y & \partial_X \\ 0 & 0 & \partial_{XY} & 0 & \partial_X \\ 0 & 0 & \partial_{XY} & \partial_Y & 0 \end{bmatrix}. \tag{10}$$

The matrices $\boldsymbol{\mathcal{A}}_s$ and $\mathbf{E}_s$ in Equation (7) can be defined as

$$\boldsymbol{\mathcal{A}}_s = \begin{bmatrix} \boldsymbol{\mathcal{A}}_s^1 & \mathbf{0} & \mathbf{0} & \mathbf{0} \\ \mathbf{0} & \boldsymbol{\mathcal{A}}_s^1 & \mathbf{0} & \mathbf{0} \\ \mathbf{0} & \mathbf{0} & \boldsymbol{\mathcal{A}}_s^3 & \mathbf{0} \\ \mathbf{0} & \mathbf{0} & \mathbf{0} & \boldsymbol{\mathcal{A}}_s^4 \end{bmatrix}, \boldsymbol{E}_s = \begin{bmatrix} \boldsymbol{E}_s^1 \\ \boldsymbol{E}_s^2 \\ \boldsymbol{E}_s^3 \\ \boldsymbol{E}_s^4 \end{bmatrix}. \tag{11}$$

The classical and generalized constitutive relations for the stress and double stress vectors are defined in a similar way, based on Equation (3):

$$\boldsymbol{\sigma} = \begin{bmatrix} \sigma_{XX} \\ \sigma_{YY} \\ \sigma_{XY} \\ \tau_{XZ} \\ \tau_{YZ} \end{bmatrix} = \boldsymbol{C}\boldsymbol{\varepsilon} \quad \Sigma = \begin{bmatrix} \boldsymbol{\Sigma}_1 \\ \boldsymbol{\Sigma}_2 \\ \boldsymbol{\Sigma}_3 \\ \boldsymbol{\Sigma}_4 \end{bmatrix} = \begin{bmatrix} \boldsymbol{\mathcal{D}}_1 & \mathbf{0} & \mathbf{0} & \mathbf{0} \\ \mathbf{0} & \boldsymbol{\mathcal{D}}_2 & \mathbf{0} & \mathbf{0} \\ \mathbf{0} & \mathbf{0} & \boldsymbol{\mathcal{D}}_3 & \mathbf{0} \\ \mathbf{0} & \mathbf{0} & \mathbf{0} & \boldsymbol{\mathcal{D}}_4 \end{bmatrix} \begin{bmatrix} \boldsymbol{\eta}_1 \\ \boldsymbol{\eta}_2 \\ \boldsymbol{\eta}_3 \\ \boldsymbol{\eta}_4 \end{bmatrix} = \boldsymbol{\mathcal{D}}\boldsymbol{\eta}, \tag{12}$$

where $\boldsymbol{C}$ and $\boldsymbol{\mathcal{D}}$, respectively, denote the classical and SG material stiffness matrices written as

$$\boldsymbol{C} = \begin{bmatrix} \lambda + 2\mu & \lambda & 0 & 0 & 0 \\ \lambda & \lambda + 2\mu & 0 & 0 & 0 \\ 0 & 0 & \mu & 0 & 0 \\ 0 & 0 & 0 & \mu & 0 \\ 0 & 0 & 0 & 0 & \mu \end{bmatrix}, \quad \boldsymbol{\mathcal{D}}_1 = \boldsymbol{\mathcal{D}}_2 = \begin{bmatrix} d_1 & d_4 & d_5 \\ d_4 & d_2 & d_6 \\ d_5 & d_6 & d_3 \end{bmatrix}, \boldsymbol{\mathcal{D}}_3 = \begin{bmatrix} d_2 & d_6 & 2\alpha_2 & \alpha_1/2 \\ d_6 & d_3 & \alpha_1/2 & \alpha_3/2 \\ 2\alpha_2 & \alpha_1/2 & d_2 & d_6 \\ \alpha_1/2 & \alpha_3/2 & d_6 & d_3 \end{bmatrix},$$
$$\boldsymbol{\mathcal{D}}_4 = \begin{bmatrix} \alpha_4 & \alpha_5/2 & \alpha_5/2 \\ \alpha_5/2 & \alpha_4 & \alpha_5/2 \\ \alpha_5/2 & \alpha_5/2 & \alpha_4 \end{bmatrix},$$

with

$$d_1 = 2\sum_{i=1}^{5}\alpha_i, d_2 = 2\alpha_2 + 2\alpha_4, d_3 = \frac{1}{2}(\alpha_3 + 2\alpha_4 + \alpha_5)$$
$$d_4 = \alpha_1 + 2\alpha_2, d_5 = \frac{1}{2}(\alpha_1 + 2\alpha_3), d_6 = \frac{1}{2}(\alpha_1 + 2\alpha_5) \tag{14}$$

2.3 | Hamilton's principle

Since the VDQ method is based on a variational formulation, Hamilton's principle is first formulated with strain energy $\mathfrak{U}$, kinetic energy T and the work of external loads W_{ext} in the form

$$\int_{t_1}^{t_2} (\delta T - \delta \mathfrak{U} + \delta W_{\text{ext}})\, dt = 0. \tag{15}$$

By taking the kinematic and constitutive relations of Equations (5), (7) and (12) into account, the strain energy is presented as

$$\begin{aligned} \delta \mathfrak{U} &= \int_{\Omega} \left(\delta \boldsymbol{\varepsilon}^T \boldsymbol{\sigma} + \delta \boldsymbol{\eta}^T \boldsymbol{\Sigma} \right) d\Omega = \int_{\Omega} \left(\delta \boldsymbol{\varepsilon}^T \boldsymbol{C} \boldsymbol{\varepsilon} + \delta \boldsymbol{\eta}^T \boldsymbol{\mathcal{D}} \boldsymbol{\eta} \right) d\Omega \\ &= \int_S \int_{-h/2}^{h/2} \left(\delta \boldsymbol{q}_0^T \boldsymbol{E}_c^T \boldsymbol{\mathcal{A}}_c^T \boldsymbol{C} \boldsymbol{\mathcal{A}}_c \boldsymbol{E}_c \boldsymbol{q}_0 + \delta \boldsymbol{q}_0^T \boldsymbol{E}_s^T \boldsymbol{\mathcal{A}}_s^T \boldsymbol{\mathcal{D}} \boldsymbol{\mathcal{A}}_s \boldsymbol{E}_s \boldsymbol{q}_0 \right)\; dZdS \end{aligned} \tag{16}$$

or with the thickness direction resultants as

$$\delta \mathfrak{U} = \int_S \delta \boldsymbol{q}_0^T \left(\boldsymbol{E}_c^T \boldsymbol{C}^* \boldsymbol{E}_c + \boldsymbol{E}_s^T \boldsymbol{\mathcal{D}}^* \boldsymbol{E}_s \right) \boldsymbol{q}_0 \; dS \tag{17}$$

with

$$\boldsymbol{C}^* = \int_{-h/2}^{h/2} \boldsymbol{\mathcal{A}}_c^T \boldsymbol{C} \boldsymbol{\mathcal{A}}_c \; dZ, \boldsymbol{\mathcal{D}}^* = \int_{-h/2}^{h/2} \boldsymbol{\mathcal{A}}_s^T \boldsymbol{\mathcal{D}} \boldsymbol{\mathcal{A}}_s \; dZ \tag{18}$$

Accordingly, the kinetic energy takes the form

$$\delta T = \int_S \int_{-h/2}^{h/2} \delta \dot{\boldsymbol{q}}^T \boldsymbol{\mathcal{A}}_0^T \rho \boldsymbol{\mathcal{A}}_0 \dot{\boldsymbol{q}} \; dZdS = \int_S \delta \dot{\boldsymbol{q}}^T \boldsymbol{M}_0 \dot{\boldsymbol{q}} \; dS \tag{19}$$

where ρ stands for the mass density and the matrix $\mathbf{M}$ is given by

$$\boldsymbol{M}_0 = \int_{-h/2}^{h/2} \boldsymbol{\mathcal{A}}_0^T \rho \boldsymbol{\mathcal{A}}_0 dZ \tag{20}$$

Finally, the work of external loads is defined as

$$\delta W_{\text{ext}} = \int_S \delta \boldsymbol{q}^T \boldsymbol{F}_0 \; dS \tag{21}$$

3 | SOLUTION PROCEDURE

As shown in Figure 1A, the two-dimensional solution domain representing the physical midsurface of the plate is divided into a number of patches. Each patch can then be transformed into square reference domains through a mapping procedure (see Figure 1B) and the VDQ discretization method is applied to directly discretize the energy functional of the problem within each patch. Since the strain energy of the SG plate formulation contains second-order derivatives of the displacement components, C^1-continuity conditions are imposed within the solution domain. By the use of the VDQ method for each patch, the required continuity conditions are guaranteed within each patch, whereas to ensure the continuity requirements at the interfaces of the patches requires a special care: completely distinct patches, with no shared nodes, are first considered and the compatibility conditions for the values of the displacement components and their derivatives are applied by using the Lagrange multiplier technique, as detailed in what follows.

3.1 | Mapping technique

The basic idea of the multi-patch VDQ method is to divide the plate domain into patches of different shapes and to discretize the energy functional within each patch. However, the GDQ discretization procedure can be applied for structured regular domains only. Hence, the physical domain of each patch must be first transformed into a structured computational domain. To this end, as shown in Figure 2, the 8-node serendipity shape functions defined in terms of local coordinates (Ξ, Θ) are employed to approximate the global coordinates (X, Y) as

$$X = \sum_{j=1}^{8} \mathrm{N}_j(\Xi, \Theta) X_j = \mathbf{NX}, Y = \sum_{j=1}^{8} \mathrm{N}_j(\Xi, \Theta) Y_j = \mathbf{NY} \tag{22}$$

where $\mathbf{N} = \left[\mathrm{N}_1 \quad \mathrm{N}_2 \quad \dots \quad \mathrm{N}_8\right]$ is the vector of shape functions for the 8-node serendipity element, with the shape functions

$$N_1 = -\frac{1}{4}(1-\Xi)(1-\Theta)(\Xi+\Theta+1), N_2 = \frac{1}{4}(1+\Xi)(1-\Theta)(\Xi-\Theta-1)$$

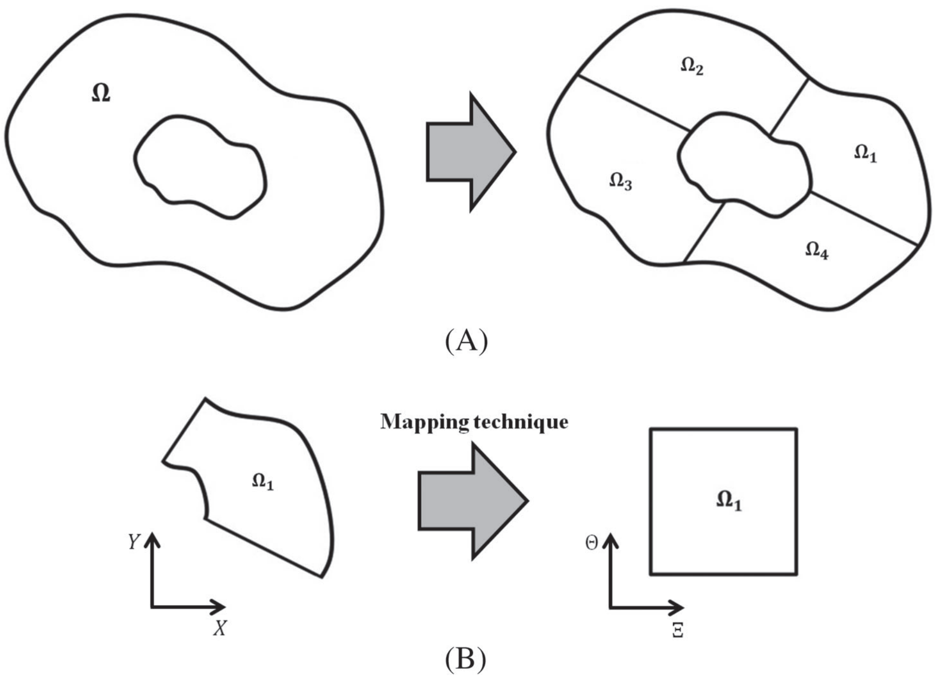

FIGURE 1 (A) Dividing the domain into patches. (B) Applying a mapping technique within each patch

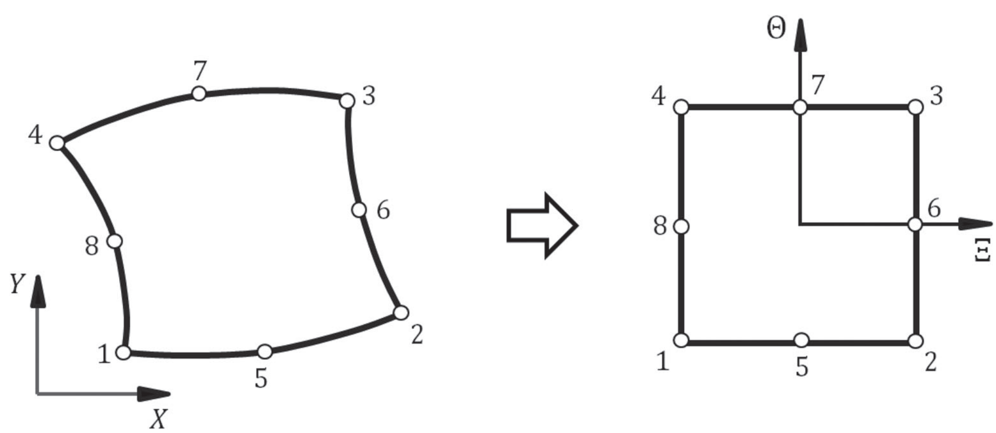

FIGURE 2 Mapping of a patch domain by using an eight-node quadrilateral finite element

$$N_3=\frac{1}{4}(1+\Xi)(1+\Theta)(\Xi+\Theta-1), N_4=\frac{1}{4}(1-\Xi)(1+\Theta)(\Theta-\Xi-1),$$
$$N_5=\frac{1}{2}\left(1-\Xi^2\right)(1-\Theta), N_6=\frac{1}{2}\left(1-\Theta^2\right)(1+\Xi),$$
$$N_7=\frac{1}{2}\left(1-\Xi^2\right)(1+\Theta), N_8=\frac{1}{2}\left(1-\Theta^2\right)(1-\Xi),$$

and $\mathbf{X}=\begin{bmatrix}X_1 & X_2 & \dots & X_8\end{bmatrix}^{\mathrm{T}}$ and $\mathbf{Y}=\begin{bmatrix}Y_1 & Y_2 & \dots & Y_8\end{bmatrix}^{\mathrm{T}}$ are the vectors of the X- and Y-coordinates of the FE nodes of each patch. By taking the chain rule into account, the formulation for the derivatives with respect to local and global coordinate systems can be expressed as

$$\begin{bmatrix}\partial_\Xi \\ \partial_\Theta\end{bmatrix}=\begin{bmatrix}\frac{\partial X}{\partial \Xi} & \frac{\partial Y}{\partial \Xi} \\ \frac{\partial X}{\partial \Theta} & \frac{\partial Y}{\partial \Theta}\end{bmatrix}\begin{bmatrix}\partial_X \\ \partial_Y\end{bmatrix}=\begin{bmatrix}\mathfrak{J}_{11} & \mathfrak{J}_{12} \\ \mathfrak{J}_{21} & \mathfrak{J}_{22}\end{bmatrix}\begin{bmatrix}\partial_X \\ \partial_Y\end{bmatrix}=\mathfrak{J}\begin{bmatrix}\partial_X \\ \partial_Y\end{bmatrix} \tag{24}$$

with $\mathfrak{J}$ as the Jacobian matrix where its components are defined by using the coordinate approximation of Equation (22) as follows:

$$\begin{aligned}\mathfrak{J}_{11}(\Xi,\Theta)&=\frac{\partial X}{\partial \Xi}=\frac{\partial \boldsymbol{N}}{\partial \Xi}\boldsymbol{X}, \mathfrak{J}_{12}(\Xi,\Theta)=\frac{\partial Y}{\partial \Xi}=\frac{\partial \boldsymbol{N}}{\partial \Xi}\boldsymbol{Y},\\ \mathfrak{J}_{21}(\Xi,\Theta)&=\frac{\partial X}{\partial \Theta}=\frac{\partial \boldsymbol{N}}{\partial \Theta}\boldsymbol{X}, \mathfrak{J}_{22}(\Xi,\Theta)=\frac{\partial Y}{\partial \Theta}=\frac{\partial \boldsymbol{N}}{\partial \Theta}\boldsymbol{Y}\end{aligned} \tag{25}$$

Now, the derivatives with respect to the (X, Y)-system can be presented in terms of the derivatives with respect to the (Ξ, Θ)-system as follows:

$$\begin{bmatrix}\partial_X \\ \partial_Y\end{bmatrix}=\boldsymbol{\mathscr{H}}\begin{bmatrix}\partial_\Xi \\ \partial_\Theta\end{bmatrix}=\begin{bmatrix}\mathscr{H}_{11} & \mathscr{H}_{12} \\ \mathscr{H}_{21} & \mathscr{H}_{22}\end{bmatrix}\begin{bmatrix}\partial_\Xi \\ \partial_\Theta\end{bmatrix} \tag{26}$$

where $\boldsymbol{\mathscr{H}}$ is defined as the inverse of the Jacobian matrix with

$$\begin{aligned}&\mathscr{H}_{11}(\Xi,\Theta)=\frac{\mathfrak{J}_{22}}{\Delta}, \mathscr{H}_{12}(\Xi,\Theta)=-\frac{\mathfrak{J}_{12}}{\Delta}, \mathscr{H}_{21}(\Xi,\Theta)=-\frac{\mathfrak{J}_{21}}{\Delta}, \mathscr{H}_{22}(\Xi,\Theta)=\frac{\mathfrak{J}_{11}}{\Delta}\\ &\Delta=\mathfrak{J}_{11}\mathfrak{J}_{22}-\mathfrak{J}_{12}\mathfrak{J}_{21}\end{aligned} \tag{27}$$

3.2 | VDQ discretization method

Since the physical domains of the patches were transformed into the corresponding structured computational domains by the mapping procedure, the VDQ discretization method can be applied: the energy functional is directly discretized with the aid of numerical differential and integral matrix operators.[9] By considering n and m grid points in the Ξ- and Θ-directions, respectively, the numerical differential matrix operators $\mathbf{D}_\Xi$ and $\mathbf{D}_\Theta$ are defined by using the GDQ technique.[1,9] With the aid of the mapping procedure defined in Equation (26), the numerical differential operators in the (X, Y)-system are expressed for each patch by

$$\begin{bmatrix}\boldsymbol{D}_X^i \\ \boldsymbol{D}_Y^i\end{bmatrix}=\mathbb{H}\begin{bmatrix}\boldsymbol{D}_\Xi \\ \boldsymbol{D}_\Theta\end{bmatrix} \tag{28}$$

where

$$\boldsymbol{\mathcal{H}}_{11}=\frac{\operatorname{diag}\left(vec\left(\mathfrak{J}_{22}\right)\right)}{\operatorname{diag}(\boldsymbol{\Delta})}, \boldsymbol{\mathcal{H}}_{12}=-\frac{\operatorname{diag}\left(vec\left(\mathfrak{J}_{12}\right)\right)}{\operatorname{diag}(\boldsymbol{\Delta})},$$
$$\boldsymbol{\mathcal{H}}_{21}=-\frac{\operatorname{diag}\left(vec\left(\mathfrak{J}_{21}\right)\right)}{\operatorname{diag}(\boldsymbol{\Delta})}, \boldsymbol{\mathcal{H}}_{22}=\frac{\operatorname{diag}\left(vec\left(\mathfrak{J}_{11}\right)\right)}{\operatorname{diag}(\boldsymbol{\Delta})}$$

in which $\mathbf{\Delta} = vec\left(\mathfrak{J}_{11} \circ \mathfrak{J}_{22} - \mathfrak{J}_{12} \circ \mathfrak{J}_{21}\right)$, whereas $\mathfrak{J}_{ij}$ are the discretized forms of $\mathfrak{J}_{ij}(\Xi, \Theta)$, $vec(\blacksquare)$ gives the pq-by-1 vector when its input is a p-by- q matrix (the vectorized form of its matrix input), and diag($\blacksquare$) returns the square diagonal p-by- p matrix when its input is a p-by-1 vector. By following the basics steps of the GDQ discretization technique, the second-order derivatives can be defined as follows:

$$\boldsymbol{D}_{XX}^{i} = \boldsymbol{D}_{X}^{i}\boldsymbol{D}_{X}^{i}, \boldsymbol{D}_{YY}^{i} = \boldsymbol{D}_{Y}^{i}\boldsymbol{D}_{Y}^{i}, \boldsymbol{D}_{XY}^{i} = \boldsymbol{D}_{X}^{i}\boldsymbol{D}_{Y}^{i} \tag{29}$$

By using the proposed differential operators, the discretized counterparts of the matrix operators related to strain and strain gradient are given by

$$\mathbb{E}_c = \begin{bmatrix} \boldsymbol{D}_X^i & \mathbf{0} & \mathbf{0} & \mathbf{0} & \mathbf{0} \\ \mathbf{0} & \boldsymbol{D}_Y^i & \mathbf{0} & \mathbf{0} & \mathbf{0} \\ \boldsymbol{D}_Y^i & \boldsymbol{D}_X^i & \mathbf{0} & \mathbf{0} & \mathbf{0} \\ \mathbf{0} & \mathbf{0} & \mathbf{0} & \boldsymbol{D}_X^i & \mathbf{0} \\ \mathbf{0} & \mathbf{0} & \mathbf{0} & \mathbf{0} & \boldsymbol{D}_Y^i \\ \mathbf{0} & \mathbf{0} & \mathbf{0} & \boldsymbol{D}_Y^i & \boldsymbol{D}_X^i \\ \mathbf{0} & \mathbf{0} & \boldsymbol{D}_X^i & \boldsymbol{D}_0 & \mathbf{0} \\ \mathbf{0} & \mathbf{0} & \boldsymbol{D}_Y^i & \mathbf{0} & \boldsymbol{D}_0 \end{bmatrix} \tag{30}$$

and

$$\mathbb{E}_s^1 = \begin{bmatrix} \boldsymbol{D}_{XX}^i & \mathbf{0} & \mathbf{0} & \mathbf{0} & \mathbf{0} \\ \mathbf{0} & \boldsymbol{D}_{XY}^i & \mathbf{0} & \mathbf{0} & \mathbf{0} \\ \boldsymbol{D}_{YY}^i & \boldsymbol{D}_{XY}^i & \mathbf{0} & \mathbf{0} & \mathbf{0} \\ \mathbf{0} & \mathbf{0} & \mathbf{0} & \boldsymbol{D}_{XX}^i & \mathbf{0} \\ \mathbf{0} & \mathbf{0} & \mathbf{0} & \mathbf{0} & \boldsymbol{D}_{XY}^i \\ \mathbf{0} & \mathbf{0} & \mathbf{0} & \boldsymbol{D}_{YY}^i & \boldsymbol{D}_{XY}^i \end{bmatrix}, \quad \mathbb{E}_s^2 = \begin{bmatrix} \mathbf{0} & \boldsymbol{D}_{YY}^i & \mathbf{0} & \mathbf{0} & \mathbf{0} \\ \boldsymbol{D}_{XY}^i & \mathbf{0} & \mathbf{0} & \mathbf{0} & \mathbf{0} \\ \boldsymbol{D}_{XY} & \boldsymbol{D}_{XX}^i & \mathbf{0} & \mathbf{0} & \mathbf{0} \\ \mathbf{0} & \mathbf{0} & \mathbf{0} & \mathbf{0} & \boldsymbol{D}_{YY}^i \\ \mathbf{0} & \mathbf{0} & \mathbf{0} & \boldsymbol{D}_{XY}^i & \mathbf{0} \\ \mathbf{0} & \mathbf{0} & \mathbf{0} & \boldsymbol{D}_{XY}^i & \boldsymbol{D}_{XX}^i \end{bmatrix}, \quad \mathbb{E}_s^3 = \begin{bmatrix} \mathbf{0} & \mathbf{0} & \mathbf{0} & \boldsymbol{D}_X^i & \mathbf{0} \\ \mathbf{0} & \mathbf{0} & \boldsymbol{D}_{XX}^i & \boldsymbol{D}_X^i & \mathbf{0} \\ \mathbf{0} & \mathbf{0} & \mathbf{0} & \mathbf{0} & \boldsymbol{D}_Y^i \\ \mathbf{0} & \mathbf{0} & \boldsymbol{D}_{YY}^i & \mathbf{0} & \boldsymbol{D}_Y^i \end{bmatrix},$$
$$\mathbb{E}_s^4 = \begin{bmatrix} \mathbf{0} & \mathbf{0} & \mathbf{0} & \boldsymbol{D}_Y^i & \boldsymbol{D}_X^i \\ \mathbf{0} & \mathbf{0} & \boldsymbol{D}_{XY}^i & \mathbf{0} & \boldsymbol{D}_X^i \\ \mathbf{0} & \mathbf{0} & \boldsymbol{D}_{XY}^i & \boldsymbol{D}_Y^i & \mathbf{0} \end{bmatrix} \tag{31}$$

By following the fundamentals of the VDQ method[9] and by using the discretized classical and SG operators presented in Equations (30) and (31), along with considering the formulations given in Equations (17), (19), and (21), the discretized forms of the strain energy, kinetic energy, and the work of external forces can be represented as follows:

$$\delta\mathfrak{U} = \delta{\mathbb{q}_0^i}^T \left(\mathbb{E}_c^T \mathbb{C}^* \mathbb{E}_c + \mathbb{E}_s^T \mathbb{D}^* \mathbb{E}_s\right) \mathbb{q}_0^i \tag{32}$$

$$\delta T = \delta{\dot{\mathbb{q}}_0^i}^T \mathbb{M}_0 \dot{\mathbb{q}}_0^i \tag{33}$$

$$\delta W_{\text{ext}} = \delta{\mathbb{q}_0^i}^T \mathbb{F}_0 \tag{34}$$

in which

$$\mathbb{C}^* = \boldsymbol{C}^* \otimes \mathbb{S}_{XY}, \mathbb{D}^* = \boldsymbol{D}^* \otimes \mathbb{S}_{XY}, \mathbb{M}_0 = \boldsymbol{M}_0 \otimes \mathbb{S}_{XY}, \mathbb{F}_0 = \boldsymbol{F}_0 \otimes \overline{\mathbb{S}}_{XY} \tag{35}$$

where $\mathbb{S}_{XY} = \mathbf{\Delta}\ \mathrm{diag}\left(\mathbf{S}_Y \otimes \mathbf{S}_X\right)$ is the diagonal numerical integral matrix operator with $\mathbf{S}_X$ and $\mathbf{S}_Y$ as the vectors of numerical integral operators in the X- and Y-directions, defined based on the Taylor series and GDQ operators.[9,16] It is noted that $\overline{\mathbb{S}}_{XY} = \text{diag}\,(\mathbb{S}_{XY})$. Besides, $\mathbb{q}_0^i$ is the vector of unknows at grid points for the ith patch. It should be also pointed out that the operator $\otimes$ stands for the Kronecker product.

Now, substituting Equations (32)–(34) into Hamilton's principle of Equation (15) gives

$$\int_{t_1}^{t_2} \left(\delta \mathbb{q}_0^{i\,T} \mathbb{M}_0 \ddot{\mathbb{q}}_0^i - \delta \mathbb{q}_0^{i\,T} \left(\mathbb{E}_c^T \mathbb{C}^* \mathbb{E}_c + \mathbb{E}_s^T \mathbb{D}^* \mathbb{E}_s \right) \mathbb{q}_0^i + \delta \mathbb{q}_0^{i\,T} \mathbb{F}_0 \right) dt = 0 \tag{36}$$

This results in the following equation of motion for each patch:

$$\mathbb{M}_i \ddot{\mathbb{q}}_0^i + \mathbb{K}_i \mathbb{q}_0^i = \mathbb{F}_i \tag{37}$$

with

$$\mathbb{M}_i = \mathbb{M}_0, \mathbb{K}_i = \mathbb{E}_c^T \mathbb{C}^* \mathbb{E}_c + \mathbb{E}_s^T \mathbb{D}^* \mathbb{E}_s, \mathbb{F}_i = \mathbb{F}_0 \tag{38}$$

where $\mathbb{M}_i$ and $\mathbb{K}_i$ are the mass and stiffness matrices, while $\mathbb{F}_i$ stands for the force vector of the ith patch. It is noted that the subscript i denotes the correspondence to patch number i. Since distinct patches with no shared nodes are considered, the equations of motion of the plate can be represented as

$$\begin{bmatrix} \mathbb{M}_1 & \mathbf{0} & \mathbf{0} & \mathbf{0} \\ \mathbf{0} & \mathbb{M}_2 & \mathbf{0} & \mathbf{0} \\ \mathbf{0} & \mathbf{0} & \ddots & \mathbf{0} \\ \mathbf{0} & \mathbf{0} & \mathbf{0} & \mathbb{M}_p \end{bmatrix} \begin{bmatrix} \ddot{\mathbb{q}}_0^1 \\ \ddot{\mathbb{q}}_0^2 \\ \vdots \\ \ddot{\mathbb{q}}_0^p \end{bmatrix} + \begin{bmatrix} \mathbb{K}_1 & \mathbf{0} & \mathbf{0} & \mathbf{0} \\ \mathbf{0} & \mathbb{K}_2 & \mathbf{0} & \mathbf{0} \\ \mathbf{0} & \mathbf{0} & \ddots & \mathbf{0} \\ \mathbf{0} & \mathbf{0} & \mathbf{0} & \mathbb{K}_p \end{bmatrix} \begin{bmatrix} \mathbb{q}_0^1 \\ \mathbb{q}_0^2 \\ \vdots \\ \mathbb{q}_0^p \end{bmatrix} = \begin{bmatrix} \mathbb{F}_1 \\ \mathbb{F}_2 \\ \vdots \\ \mathbb{F}_p \end{bmatrix} \tag{39}$$

where p is the number of patches. Finally, Equation (39) can be represented as follows:

$$\mathbb{M} \ddot{\mathbb{q}}_0 + \mathbb{K} \mathbb{q}_0 = \mathbb{F} \tag{40}$$

3.3 | Compatibility conditions

Since the SG shear deformation plate problem requires C^1-continuity conditions due to the existence of second-order derivatives of the displacement components in the strain energy (Equations (10) and (17)), the corresponding compatibility conditions should be applied at the interfaces of the adjacent patches for values of the displacement components (the first line of Equation (41)), their first-order derivatives (the second and third lines of Equation (41)), and their mixed second-order derivatives (the fourth line of Equation (41)):

$$\begin{cases} \mathbb{q}_0^i - \mathbb{q}_0^j = \mathbf{0} \\ \boldsymbol{D}_X^i \mathbb{q}_0^i - \boldsymbol{D}_X^j \mathbb{q}_0^j = \mathbf{0} \\ \boldsymbol{D}_Y^i \mathbb{q}_0^i - \boldsymbol{D}_Y^j \mathbb{q}_0^j = \mathbf{0} \\ \boldsymbol{D}_{XY}^i \mathbb{q}_0^i - \boldsymbol{D}_{XY}^j \mathbb{q}_0^j = \mathbf{0} \end{cases} \quad \text{on } B_{i,j} \tag{41}$$

where $B_{i,j}$ is the interface between patches i and j. Indeed, the compatibility conditions of Equation (41) should be applied for the grid points on all interfaces of the adjacent patches. Applying the first three compatibility conditions of Equation (41) results in quasi-confirming continuity only. It is worth noting, however, that our results indicate that considering the first three conditions can lead to accurate results, and the last condition does not considerably affect the performance of the method. For imposing the conditions of Equation (41), the standard Lagrange multiplier technique has been employed in the present study. By following the fundamentals of the standard Lagrange multiplier technique, the total energy related to the constraints in Equation (41) is added to the energy functional of the structure, and accordingly, the final governing equations are modified. To implement this idea, first, the total differential operators of the whole structure should be defined by using those of each patch as follows:

$$\boldsymbol{D}_X=\begin{bmatrix}\boldsymbol{D}_X^1 & \mathbf{0} & \mathbf{0} & \mathbf{0}\\ \mathbf{0} & \boldsymbol{D}_X^2 & \mathbf{0} & \mathbf{0}\\ \mathbf{0} & \mathbf{0} & \ddots & \mathbf{0}\\ \mathbf{0} & \mathbf{0} & \mathbf{0} & \boldsymbol{D}_X^p\end{bmatrix},\boldsymbol{D}_Y=\begin{bmatrix}\boldsymbol{D}_Y^1 & \mathbf{0} & \mathbf{0} & \mathbf{0}\\ \mathbf{0} & \boldsymbol{D}_Y^2 & \mathbf{0} & \mathbf{0}\\ \mathbf{0} & \mathbf{0} & \ddots & \mathbf{0}\\ \mathbf{0} & \mathbf{0} & \mathbf{0} & \boldsymbol{D}_Y^p\end{bmatrix},\boldsymbol{D}_{XY}=\begin{bmatrix}\boldsymbol{D}_{XY}^1 & \mathbf{0} & \mathbf{0} & \mathbf{0}\\ \mathbf{0} & \boldsymbol{D}_{XY}^2 & \mathbf{0} & \mathbf{0}\\ \mathbf{0} & \mathbf{0} & \ddots & \mathbf{0}\\ \mathbf{0} & \mathbf{0} & \mathbf{0} & \boldsymbol{D}_{XY}^p\end{bmatrix} \tag{42}$$

Also, the identity matrix $\mathbf{I} \cong \mathbf{I}_{5nm\times 5nm}$ is defined. Now, the compatibility constraints defined in Equation (41) for the interface between patches i and j (let us call it interface number r) can be represented by

$$\mathbb{G}_r\mathbb{q}=\mathbf{0},\mathbb{G}_r=\begin{bmatrix}\boldsymbol{I}^{B_i}-\boldsymbol{I}^{B_j}\\ \boldsymbol{D}_X^{B_i}-\boldsymbol{D}_X^{B_j}\\ \boldsymbol{D}_Y^{B_i}-\boldsymbol{D}_Y^{B_j}\\ \boldsymbol{D}_{XY}^{B_i}-\boldsymbol{D}_{XY}^{B_j}\end{bmatrix} \tag{43}$$

where, for instance, $\mathbf{I}^{\mathrm{B}_i}$ and $\mathbf{D}_X^{\mathrm{B}_i}$ are the rows of matrices $\mathbf{I}$ and $\mathbf{D}_X$ related to the grid points of domain i located on the intended interface (which is called interface number r here). The same notation is considered for $\mathbf{D}_Y^{\mathrm{B}_i}$, $\mathbf{D}_{XY}^{\mathrm{B}_i}$ and related matrices in domain j. Next, if the number of interfaces is R, the total compatibility constraints can be written as

$$\mathbb{G}\mathbb{q}=\mathbf{0},\mathbb{G}=\begin{bmatrix}\mathbb{G}_1\\ \mathbb{G}_2\\ \vdots\\ \mathbb{G}_R\end{bmatrix} \tag{44}$$

and by following the standard Lagrange multiplier technique, the total energy of the constraints is given by $(\mathbb{G}\mathbb{q})^{\mathrm{T}}\lambda$, where λ denotes the vector of Lagrange multipliers and the governing equation of Equation (40) can be updated as

$$\begin{bmatrix}\mathbb{M} & \mathbf{0}\\ \mathbf{0} & \mathbf{0}\end{bmatrix}\begin{Bmatrix}\ddot{\mathbb{q}}_0\\ \lambda\end{Bmatrix}+\begin{bmatrix}\mathbb{K} & \mathbb{G}^T\\ \mathbb{G} & \mathbf{0}\end{bmatrix}\begin{Bmatrix}\mathbb{q}_0\\ \lambda\end{Bmatrix}=\begin{Bmatrix}\mathbb{F}\\ \mathbf{0}\end{Bmatrix} \tag{45}$$

To elaborate further on the idea, as an example let us consider the square plate shown in Figure 3A divided into two rectangular patches (Figure 3B), where each patch is discretized by using 7×7 grid points. As can be seen, there is just one interface and by following Equations (41) and (42), the compatibility conditions can be given as

$$\mathbb{G}=\mathbb{G}_1=\begin{bmatrix}\boldsymbol{I}^{B_1}-\boldsymbol{I}^{B_2}\\ \boldsymbol{D}_X^{B_1}-\boldsymbol{D}_X^{B_2}\\ \boldsymbol{D}_Y^{B_1}-\boldsymbol{D}_Y^{B_2}\\ \boldsymbol{D}_{XY}^{B_1}-\boldsymbol{D}_{XY}^{B_2}\end{bmatrix} \tag{46}$$

where the corresponding grid points at edges B_1 and B_2 are marked in Figure 3C. Indeed, by the use of the number of grid points on edge B_1, one can select the related rows in matrices $\mathbf{I}$, $\mathbf{D}_X$, $\mathbf{D}_Y$, and $\mathbf{D}_{XY}$ to define $\mathbf{I}^{\mathrm{B}_1}$, $\mathbf{D}_X^{\mathrm{B}_1}$, $\mathbf{D}_Y^{\mathrm{B}_1}$, and $\mathbf{D}_{XY}^{\mathrm{B}_1}$, respectively. The same approach is used for edge B_2.

3.4 | Boundary conditions

In addition to the compatibility conditions, the specified boundary conditions should be applied at the external edges solution domain. In the present SG plate formulation, higher-order boundary conditions might need to be imposed in

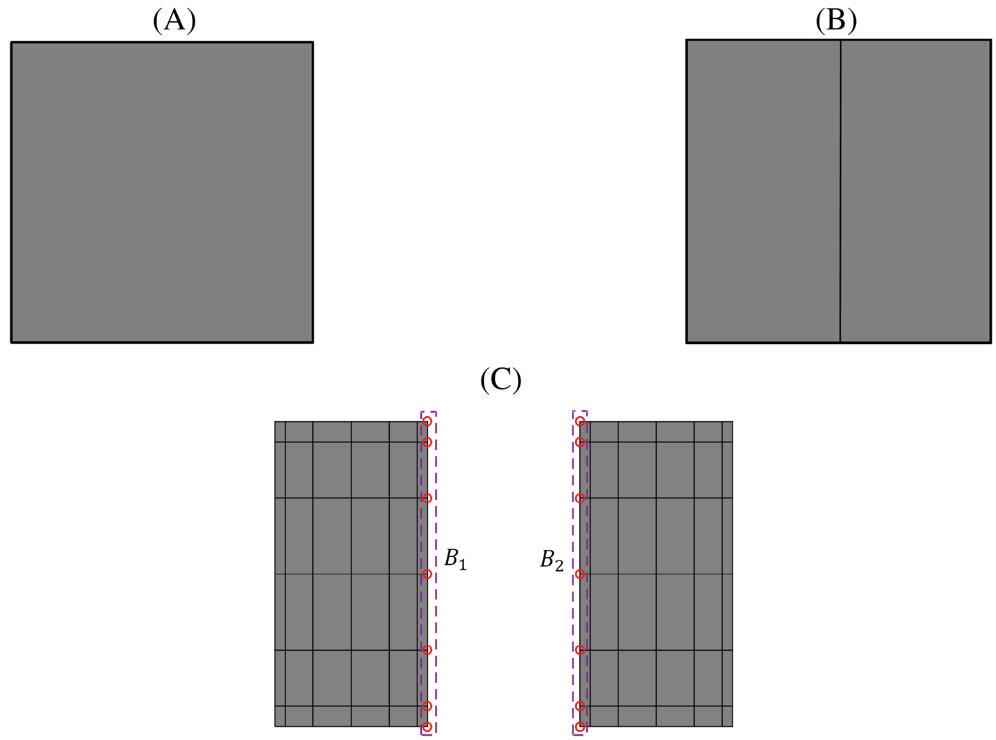

FIGURE 3 (A) Schematic view of a square plate (B) a square plate divided into two patches (C) discretization and grid points on the interface

addition to the standard classical ones. On the other hand, within the variational formulation, this concerns the essential (displacement) boundary conditions only. In the present study, the following clamped and simply supported boundary conditions are studied:

$$\text{clamped:} \begin{cases} \overline{U} = \overline{V} = W = \overline{\Psi} = \overline{\Phi} = 0, \\ \frac{\partial Q}{\partial n} = \frac{\partial Q}{\partial t} = 0, \qquad (Q = U, V, W, \Psi, \Phi) \end{cases}$$
$$\text{simply supported} : \overline{U} = \overline{V} = W = \overline{\Phi} = 0, \tag{47}$$

with the notation

$$\overline{U} = n_X U + n_Y V, \overline{V} = -n_Y U + n_X V,$$
$$\overline{\Psi} = n_X \Psi + n_Y \Phi, \overline{\Phi} = -n_Y \Psi + n_X \Phi,$$
$$\frac{\partial Q}{\partial n} = n_X \frac{\partial Q}{\partial X} + n_Y \frac{\partial Q}{\partial Y}, \frac{\partial Q}{\partial t} = -n_Y \frac{\partial Q}{\partial X} + n_X \frac{\partial Q}{\partial Y}, \quad (Q = U, V, W, \Psi, \Phi) \tag{48}$$

in which n_X, n_Y stand for the components of the outward unit normal vector of the boundaries. The standard penalty approach is utilized in this study to impose the boundary conditions.

4 | NUMERICAL RESULTS

A wide range of numerical examples is represented in this section to address the accuracy and numerical efficiency of the proposed solution method. Since the main point is to explore the performance of the numerical solution method, and not to focus on the constitutive relations of the SG theory, the following assumptions are adopted:

$$\alpha_1 = \mu \left(l_2^2 - \frac{4}{15} l_1^2 \right), \alpha_2 = \mu \left(l_0^2 - \frac{1}{15} l_1^2 - \frac{1}{2} l_2^2 \right), \alpha_3 = -\mu \left(\frac{4}{15} l_1^2 + \frac{1}{2} l_2^2 \right)$$

$$\alpha_4 = \mu\left(\frac{1}{3}l_1^2 + l_2^2\right), \alpha_5 = \mu\left(\frac{2}{3}l_1^2 - l_2^2\right) \tag{49}$$

where l_0, l_1, l_2 stand for the material length scale parameters of the so-called modified SG theory. The non-dimensional forms of the maximum deflection and natural frequency, $W_{\max}/h$ and $\overline{\omega} = \omega\frac{a^2}{2\pi}\sqrt{\frac{\rho h(1-\nu^2)}{Eh^3}}$, respectively, are reported for the computational results, with h denoting the thickness of the plate. The following values of material properties for Young's modulus, mass density, and Poisson's ratio are chosen for the benchmarks:

$$E = 1.44\ \text{GPa}, \rho = 1220\frac{\text{kg}}{\text{m}^3}, \nu = 0.38. \tag{50}$$

As the main advantage of the developed solution model is to deal with the SG plate problem for complex non-convex domains, both convex and non-convex domains are chosen for the benchmark study: square, square with a square cutout, irregular shape (a triangle connected to a semicircle with an elliptical cutout); as shown in Figure 4A–C, respectively.

The common geometrical parameters are $a/h = 10$ and $l_0 = l_1 = l_2 = h/2$, while for the square with a square cutout $b/a = 0.2$ and for the irregular plate $b/a = 0.3, c/a = 0.2$. To generate the results for bending analysis, a uniformly distributed load (q) is set to follow the non-dimensional relation $qa^4/Eh^4 = 400$.

4.1 | Square plate

To assess the applicability of the method in the simple square domain, three patterns of patches are considered: two identical rectangles (2 patches), four different rectangles (4 unstructured patches), and four identical squares (4 structured patches); as shown in Figure 5A–C, respectively.

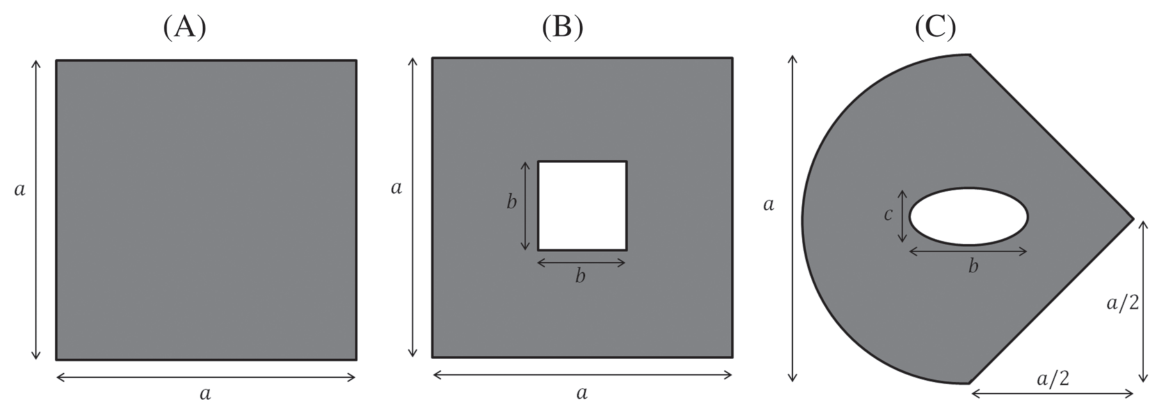

FIGURE 4 Different plate shapes and the related dimensions: (A) Square (B) square with a square cutout (C) triangle connected to a semicircle with an elliptical cutout

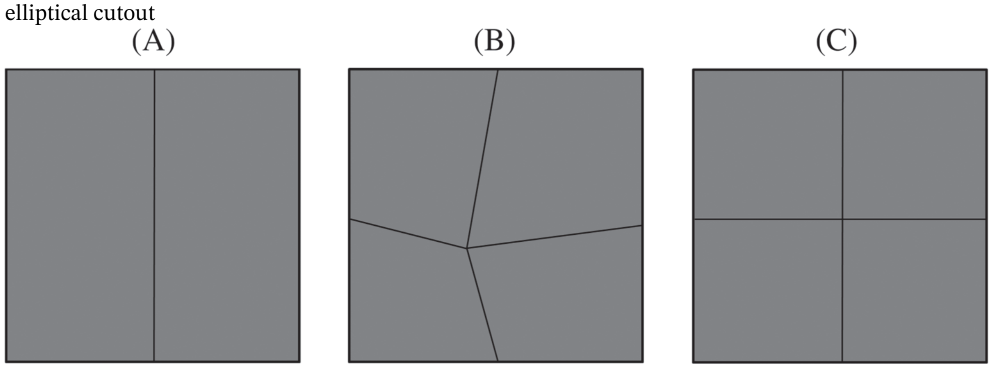

FIGURE 5 Three patterns of patches for the square plate: (A) Two identical rectangles (B) four different rectangles (C) four identical squares

The convergence results for the relative error of the maximum deflection and the first two natural frequencies are illustrated in Figures 6 and 7 for the three different patterns of patches for fully clamped and fully simply supported boundary conditions, respectively. The relative errors are based on the relation $(V - V_c)/V_c$ where V stands for the value of the non-dimensional maximum deflection or natural frequencies, with the subscript c denoting a converged reference value. For comparisons, the convergence rates (Order 1, Order 2, Order 3) are plotted aside the results.

The results of Figure 6 indicate that the convergence rate for the clamped square is between orders 3 and 4. The results in Figure 7 show that the convergence rate for the simply supported square is between orders 1 and 2 with two patches and with four unstructured patches, whereas in the case of four structured patches, the corresponding rate is between orders 2 and 3.

To give more details on the convergence properties and to perform a comparison with a FE analysis, the variations of the non-dimensional maximum deflections and the first four natural frequencies are represented in Tables 1 and 2, respectively, for different patch patterns, numbers of grid points, and boundary conditions. The converged results are also compared with the corresponding values from a FE analysis. The FE results are based on the higher-order six-node triangular element (see Figure 8) developed by the authors in the previously published articles[38,43]: the values of the field variables and their first-order derivatives are considered as the nodal values to respond to the continuity requirements. A Gauss quadrature is used for the numerical integration of the stiffness and mass matrices.

It is observed that by the increase of the numbers of grid points within each patch the results rapidly converge. An interesting point here is that even considering a small number of grid points (for instance, $n = m = 9$) leads to fairly

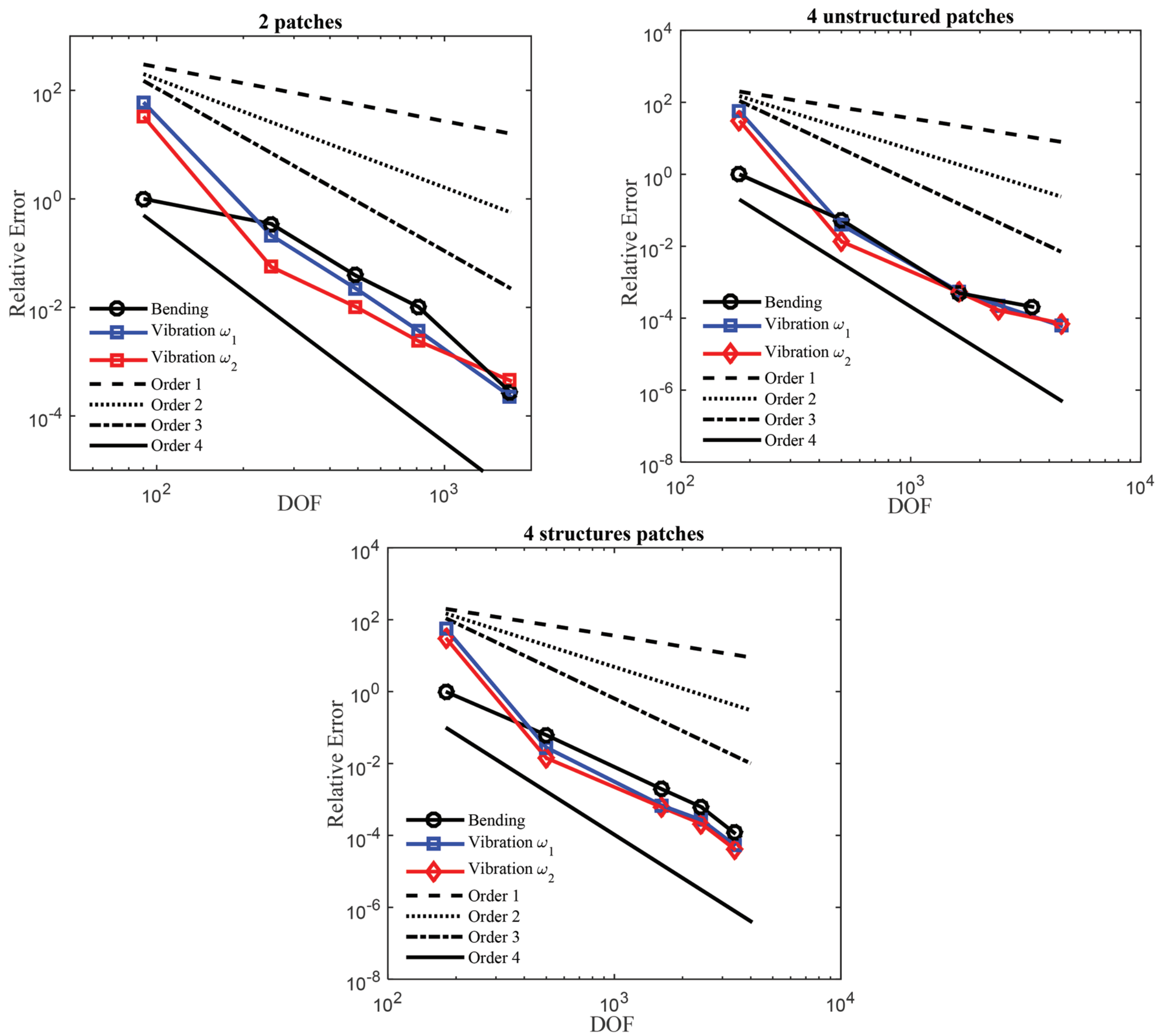

FIGURE 6 Convergence results for bending and vibration analysis of a clamped square plate

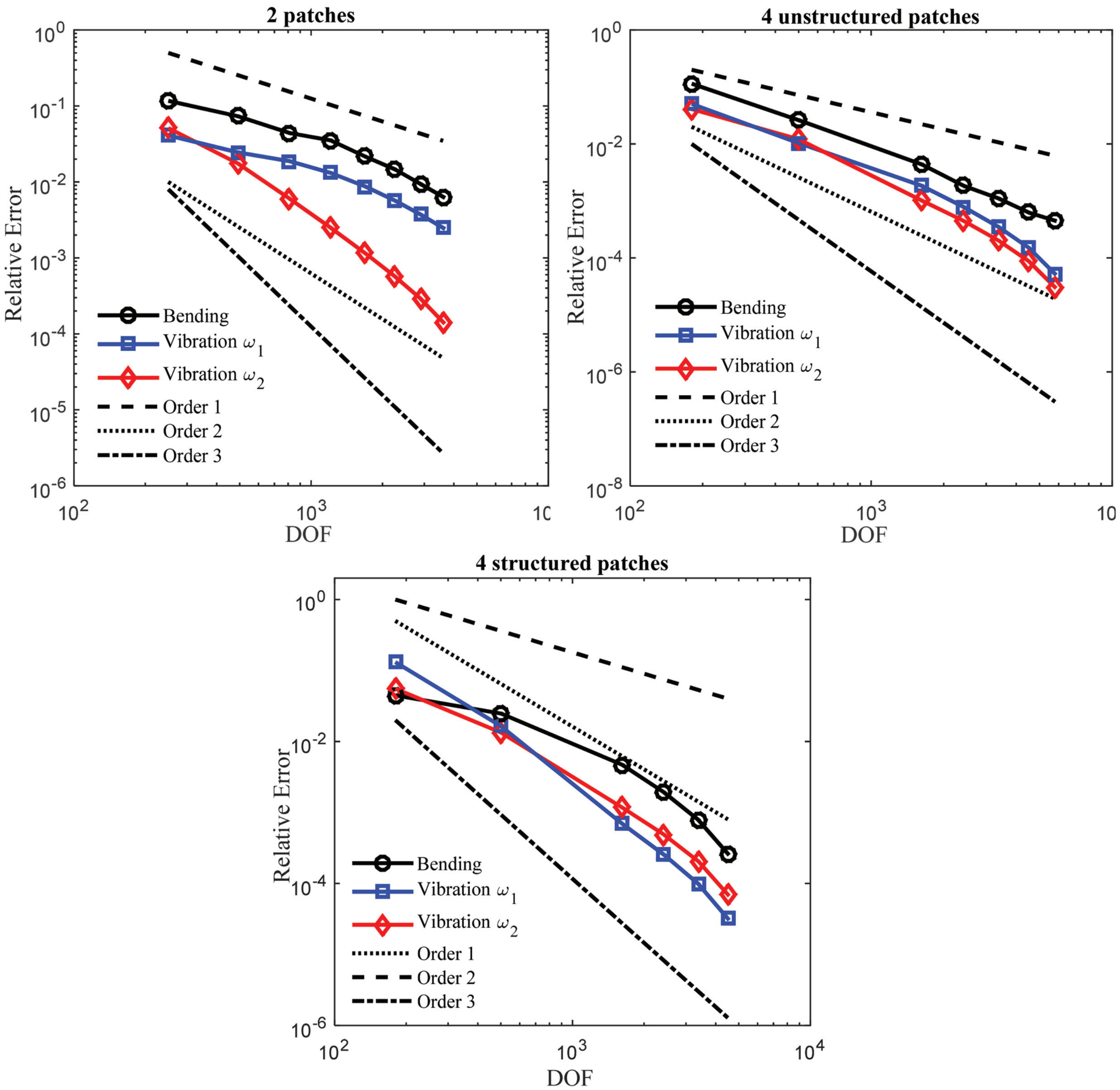

FIGURE 7 Convergence results for bending and vibration analysis of a simply supported square plate

TABLE 1 Convergence of the non-dimensional maximum deflection for a square plate

	Clamped			Simply supported		
$n = m$	2 patches	4 unstructured patches	4 structured patches	2 patches	4 unstructured patches	4 structured patches
5	1.199	1.731	1.718	5.282	4.94	4.938
9	1.814	1.841	1.835	5.031	4.835	4.841
11	1.833	1.835	1.833	4.988	4.805	4.828
13	1.832	1.832	1.832	4.922	4.819	4.822
15	1.832	1.831	1.832	4.889	4.811	4.82
17	1.832	1.831	1.832	4.863	4.816	4.818
FEM	1.829			4.810		

TABLE 2 Convergence of the non-dimensional natural frequencies for a square plate

		Clamped			Simply supported		
	$n = m$	2 patches	4 unstructured patches	4 structured patches	2 patches	4 unstructured patches	4 structured patches
$\overline{\omega}_1$	5	3.307	2.832	2.802	1.590	1.650	1.651
	9	2.736	2.724	2.724	1.636	1.664	1.664
	11	2.727	2.725	2.725	1.645	1.666	1.666
	13	2.725	2.726	2.726	1.653	1.666	1.667
	15	2.726	2.726	2.726	1.658	1.667	1.667
	17	2.726	2.726	2.726	1.661	1.667	1.667
	FEM	2.725			1.667		
$\overline{\omega}_2$	5	5.150	4.945	4.948	3.496	3.624	3.636
	9	4.865	4.875	4.875	3.663	3.665	3.681
	11	4.869	4.877	4.877	3.676	3.667	3.683
	13	4.875	4.878	4.878	3.681	3.668	3.684
	15	4.877	4.878	4.878	3.683	3.668	3.685
	17	4.878	4.878	4.878	3.684	3.669	3.685
	FEM	4.875			3.685		
$\overline{\omega}_3$	5	6.160	4.969	4.948	4.081	3.634	3.653
	9	4.881	4.876	4.875	3.686	3.681	3.681
	11	4.878	4.877	4.877	3.685	3.684	3.683
	13	4.878	4.878	4.878	3.685	3.685	3.684
	15	4.878	4.878	4.878	3.685	3.685	3.685
	17	4.878	4.878	4.878	3.685	3.685	3.685
	FEM	4.875			3.685		
$\overline{\omega}_4$	5	6.385	6.292	6.295	5.395	5.311	5.317
	9	6.222	6.229	6.229	5.407	5.400	5.402
	11	6.227	6.230	6.230	5.406	5.403	5.405
	13	6.229	6.230	6.230	5.406	5.404	5.405
	15	6.230	6.230	6.230	5.406	5.404	5.406
	17	6.230	6.230	6.230	5.406	5.404	5.406
	FEM	6.226			5.404		

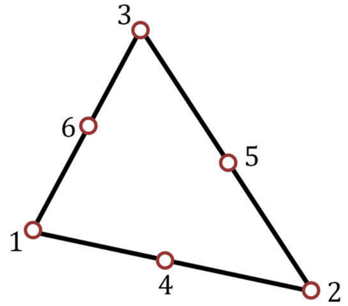

$$\left\{\begin{array}{l} \varphi(\mathbf{x}_i) = \Phi_i^0 \\ \dfrac{\partial\varphi(\mathbf{x}_i)}{\partial x} = \Phi_i^x \\ \dfrac{\partial\varphi(\mathbf{x}_i)}{\partial y} = \Phi_i^y \end{array}\right\}$$

FIGURE 8 Description of the quasi-conforming 6-node triangular element accurate results. Indeed, the convergence of the results can be obtained by either increasing the numbers of grid points or the numbers of patches. A close agreement with the FE results can be observed as well. It is also worth mentioning that according to the results in Figures 6 and 7 and Tables 1 and 2, it is found that by considering the total DOFs of around 800, it is possible to have accurate results with less than 1% relative error, while the corresponding FE results are obtained by using more than 6000 DOFs. This clearly shows the advantages of the proposed numerical strategy in terms of relative computational performance in comparison to the FE analysis. The deflection distributions and vibrational mode shapes of the square plate for different patch patterns and boundary conditions are demonstrated in Figures 9–12.

In addition, to demonstrate the importance of the applied higher-order compatibility conditions (defined in Equation (41)) and to highlight the C^1-continuity conditions through the response, the distribution of the first- and second-order derivatives of the deflection for a simply supported square plate are represented in Figure 13. The results are given for the first- and second-order derivatives of the defection with respect to X and Y (i.e., $W_{,X}$, $W_{,Y}$, $W_{,XX}$, and $W_{,YY}$), and the mixed second-order derivative of the deflection ($W_{,XY}$). The smoothly continuous distributions of the derivatives ensure the required C^1-continuty conditions for the SG shear deformation plate problem.

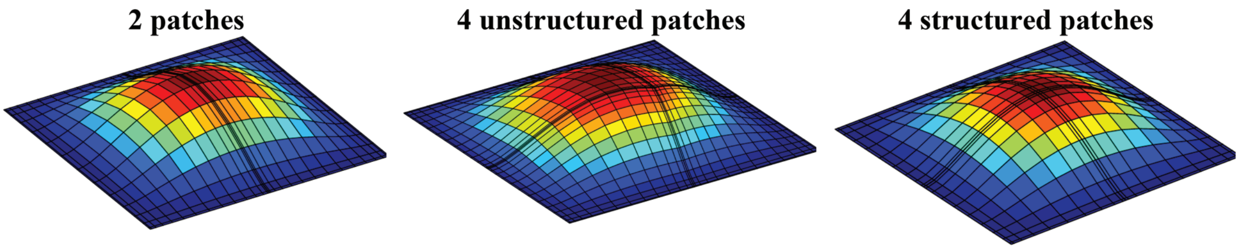

FIGURE 9 Distribution of deflection for a clamped square plate

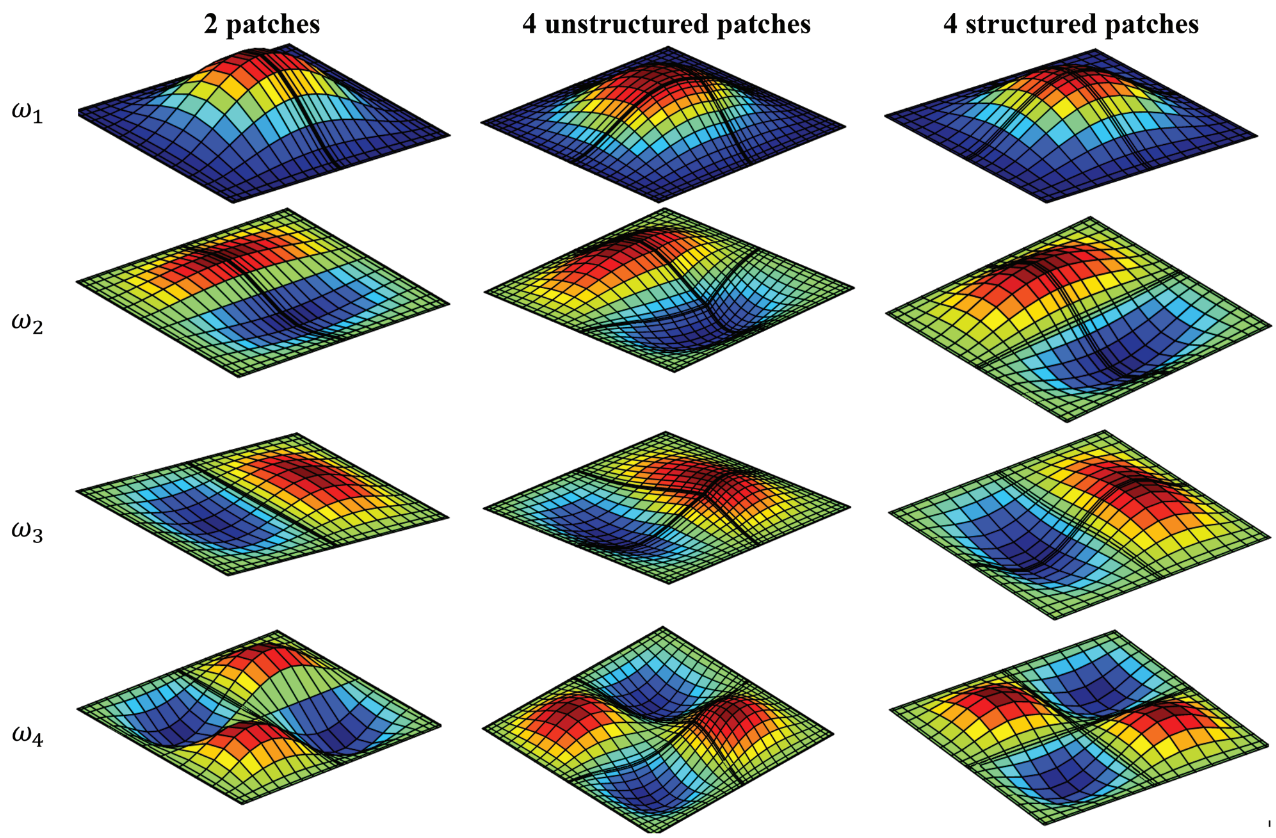

FIGURE 10 The first four vibrational mode shapes for a clamped square plate

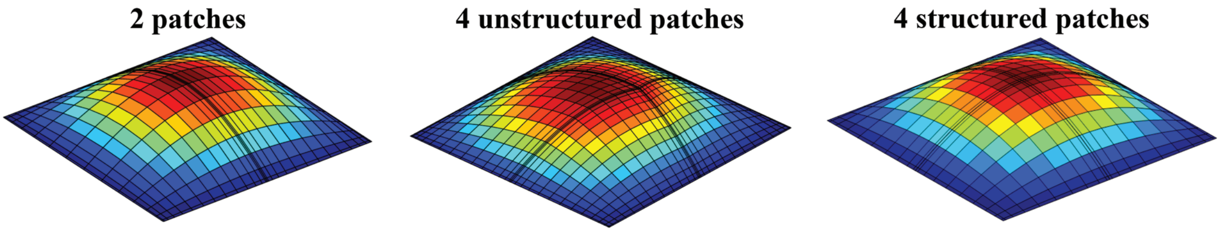

FIGURE 11 Distribution of deflection for a simply supported square plate

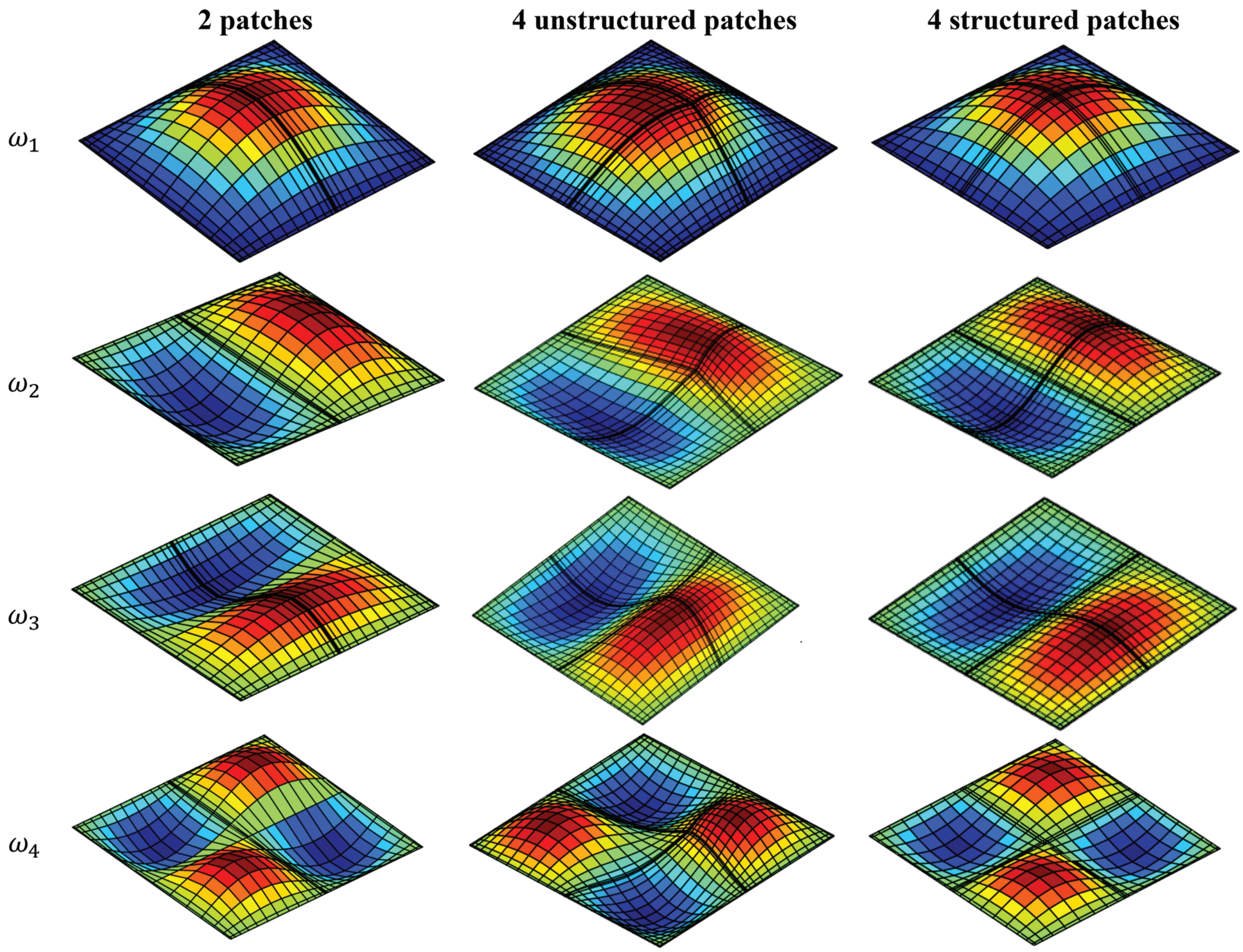

FIGURE 12 The first four vibrational mode shapes for a simply supported square plate

4.2 | Square plate with a square cutout

The numerical results of this subsection, for a square plate with a square cutout, highlight the performance of the VDQ method for more complex domains. The schematic view and geometrical parameters of the nonconvex solution are depicted in Figure 4B. In this case, two patterns of four patches and eight patches are considered, as represented in Figure 14.

The convergence studies for a square plate with a cutout with clamped and simply supported boundary supports are demonstrated in Figures 15 and 16, respectively: the variations of the relative errors of the maximum deflection and the first two natural frequencies versus the total DOF.

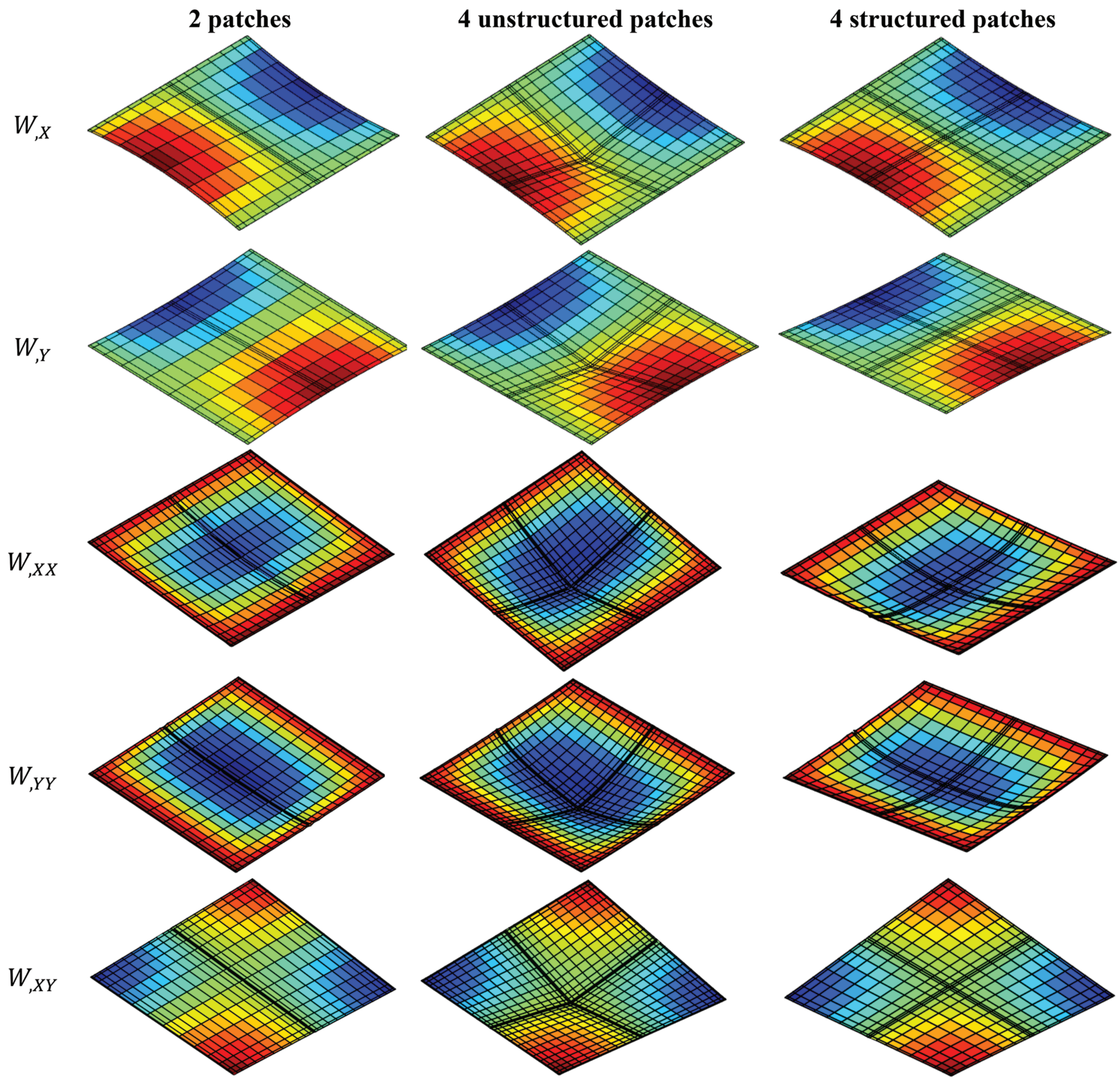

FIGURE 13 Distribution of the second-order derivatives of deflection for a simply supported square plate

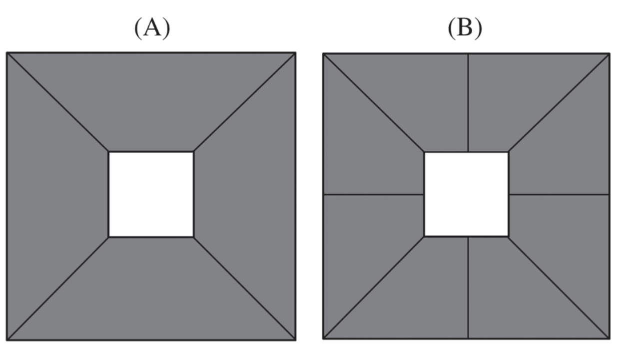

FIGURE 14 Two patch patterns for a square plate with a square cutout: (A) Four patches (B) eight patches

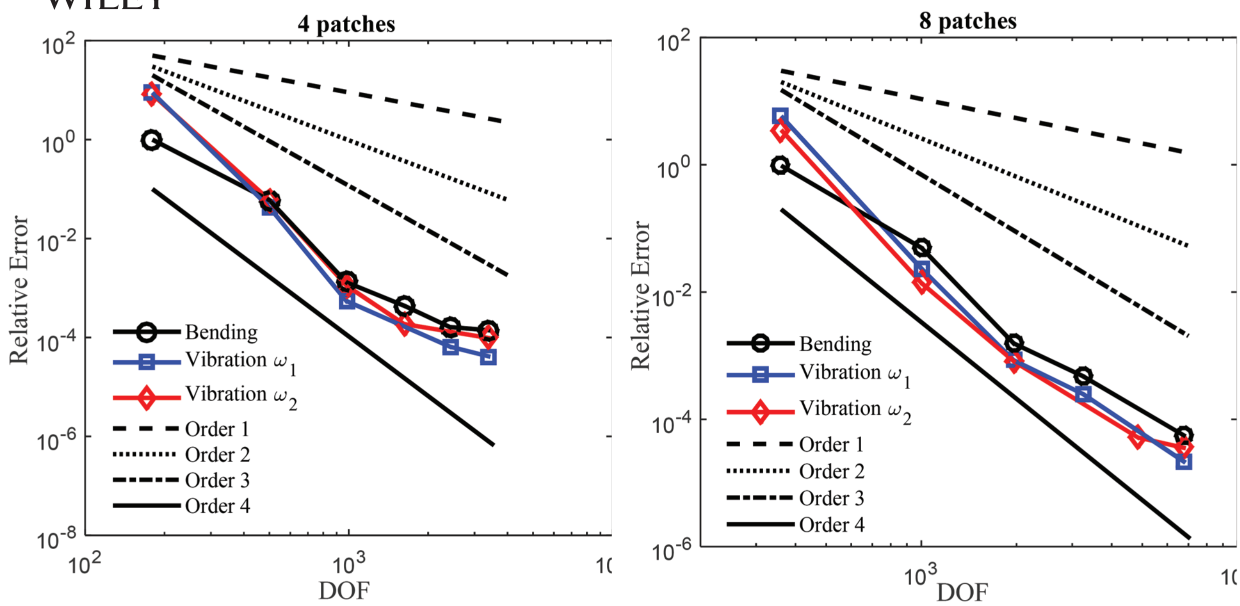

FIGURE 15 Convergence results for bending and vibration analysis of a clamped square plate with a square cutout

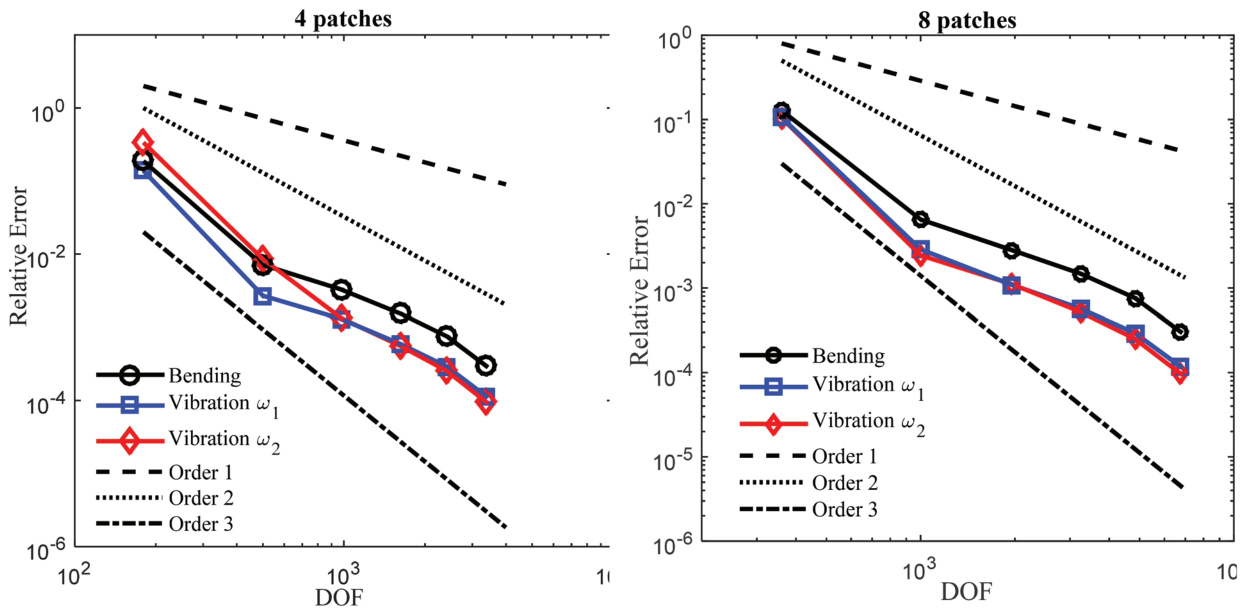

FIGURE 16 Convergence results for bending and vibration analysis of a simply supported square plate with a square cutout

TABLE 3 Convergence and comparison of the non-dimensional maximum deflection for a square plate with a cutout

	Clamped		Simply supported	
$n = m$	4 patches	8 patches	4 patches	8 patches
3	0.001	0.001	4.166	4.475
5	1.593	1.632	5.093	5.096
7	1.696	1.697	5.113	5.115
9	1.695	1.695	5.122	5.122
11	1.694	1.694	5.126	5.125
13	1.694	1.694	5.128	5.128
15	1.694	1.694	5.129	5.129
FEM	1.695		5.126	

TABLE 4 Convergence and comparison of the non-dimensional natural frequencies for a square plate with a square cutout

		Clamped		Simply supported	
	$n = m$	4 patches	8 patches	4 patches	8 patches
$\overline{\omega}_1$	3	28.563	27.430	1.893	1.839
	5	3.017	2.975	1.668	1.668
	7	2.892	2.892	1.665	1.665
	9	2.893	2.893	1.664	1.664
	11	2.894	2.894	1.664	1.664
	13	2.894	2.894	1.663	1.663
	15	2.894	2.894	1.663	1.663
	FEM	2.893		1.664	
$\overline{\omega}_2$	3	42.948	37.770	4.697	3.880
	5	4.933	4.799	3.544	3.522
	7	4.660	4.657	3.518	3.518
	9	4.655	4.655	3.516	3.516
	11	4.655	4.655	3.514	3.514
	13	4.655	4.655	3.514	3.514
	15	4.655	4.654	3.514	3.514
	FEM	4.652		3.514	
$\overline{\omega}_3$	3	42.948	37.770	4.697	3.880
	5	7.015	4.799	3.544	3.522
	7	4.660	4.657	3.518	3.518
	9	4.655	6.483	3.516	3.516
	11	4.655	4.655	3.514	3.514
	13	4.655	4.655	3.514	3.514
	15	4.654	4.654	3.514	3.514
	FEM	4.652		3.514	
$\overline{\omega}_4$	3	71.185	38.273	6.376	5.545
	5	7.015	6.926	5.298	5.233
	7	6.506	6.496	5.256	5.256
	9	6.483	6.818	5.256	5.256
	11	6.485	6.485	5.255	5.255
	13	6.485	6.485	5.255	5.255
	15	6.485	6.485	5.255	5.255
	FEM	6.481		5.254	

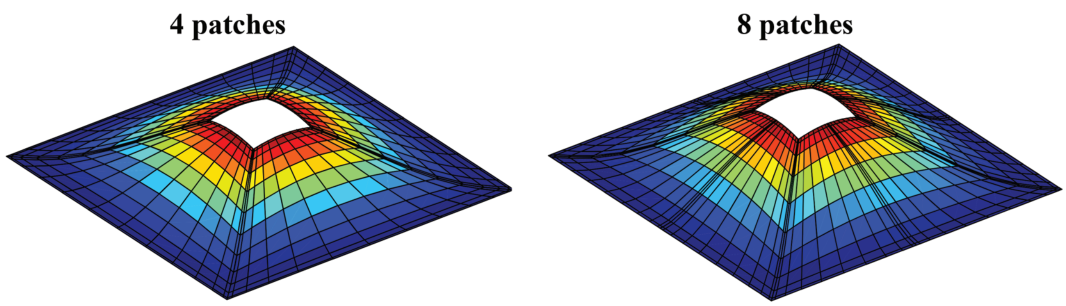

FIGURE 17 Distribution of deflection for a clamped square plate with a square cutout

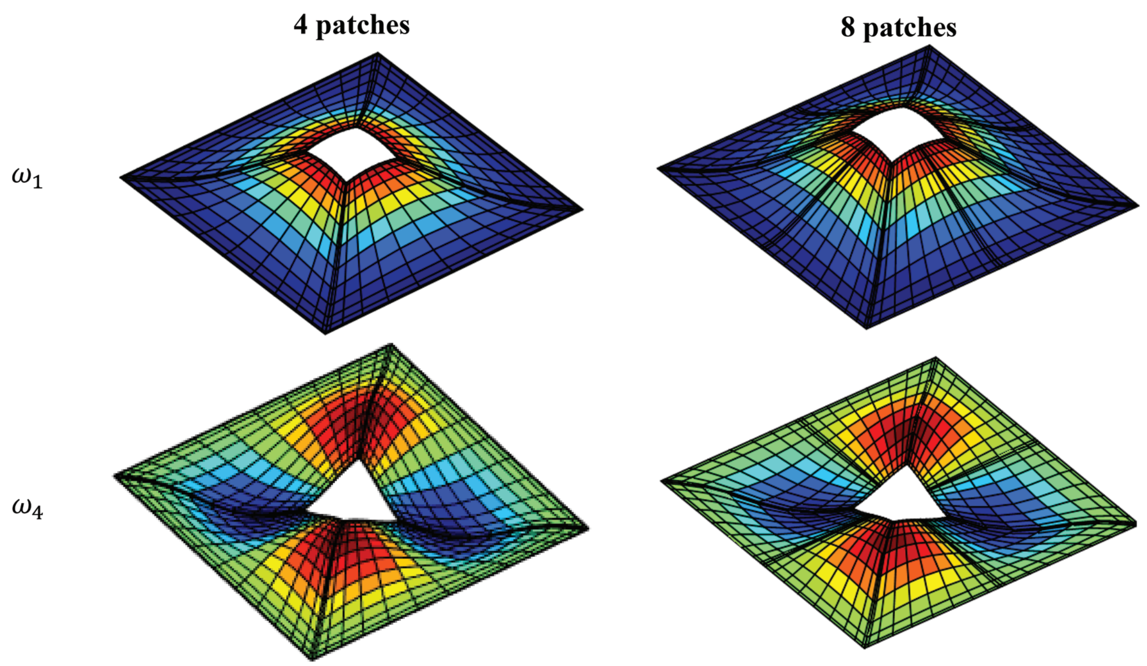

FIGURE 18 The first and fourth vibrational mode shapes for a clamped square plate with a square cutout

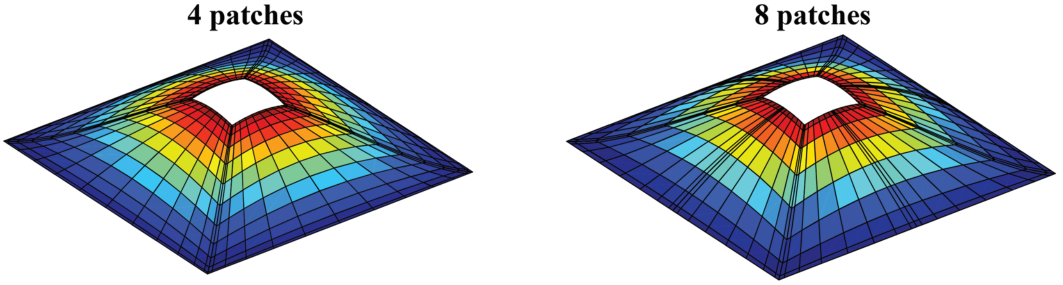

FIGURE 19 Distribution of deflection for a simply supported square plate with a square cutout

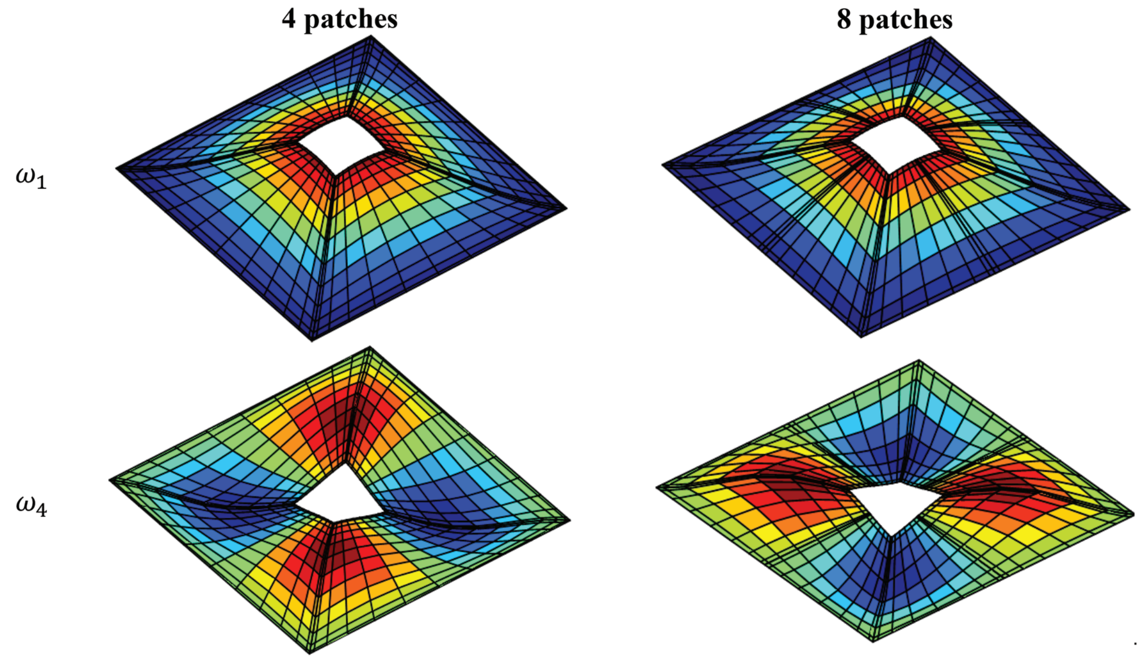

FIGURE 20 The first and fourth vibrational mode shapes for a simply supported square plate with a square cutout

In Figures 15 and 16, the relative errors are given in the form $(V - V_c)/V_c$ where V denotes the value of the non-dimensional maximum deflection or natural frequency, whereas subscript c stands for a converged value. Two subplots are presented for each case related to the two different patch patterns. For comparisons, the convergence rates (Order 1, Order 2, Order 3) are plotted aside the results. These results show the convergence curves lie between orders 2 and 3 for both patch patterns.

For more details and comparisons with FE results, the values of the non-dimensional maximum deflection and the first four natural frequencies are reported in Tables 3 and 4 for both patch patterns, different grids, and different boundary conditions. The corresponding FE results based on a higher-order six-node triangular element[38,43] are included for comparison.

The results indicate that the rapid convergence of the results for both analysis types can be obtained by increasing the number of grid points within patches. It is also found that fairly accurate results are obtained by considering only a few numbers of grid points in each direction within a patch. Quantitatively speaking, the results of Table 3 show that selecting only seven grid points in each direction of each patch ($n = m = 7$) leads to the results with a relative error less than 0.003 for simply supported boundaries and below 0.001 for clamped boundaries.

Figures 17–20 visualize the deflection distributions and vibrational mode shapes for the square plate with a cutout with two different patch patterns, for both clamped and simply supported boundary conditions. For the sake of brevity, only first and fourth mode shapes are represented. Besides, the distributions of the first- and second-order derivatives of deflection ($W_{,X}$, $W_{,Y}$, $W_{,XX}$, $W_{,YY}$, and $W_{,XY}$) are illustrated in Figure 21 for fully simply supported plate to indicate the requirements of the C^1-continuity conditions.

4.3 | Irregular plate

To show the efficiency of the multi-patch VDQ method in the bending and vibration analysis of the SG plate problem for less regular domains, we consider a domain consisting of a triangle connected to a semicircle with an elliptic cutout as shown in Figure 4C. Figure 22 shows the three different patch patterns tested: four, eight, and twelve patches.

Figure 23 shows the convergence results for the relative errors of the maximum deflection and natural frequencies for both clamped and simply supported boundary conditions. The case of four patches exhibits the lowest convergence rate which might follow from the long curved edges within the patches, which indicates the relevance of the numbers of patches. Tables 5 and 6 list the corresponding results of the non-dimensional maximum deflections and the first four

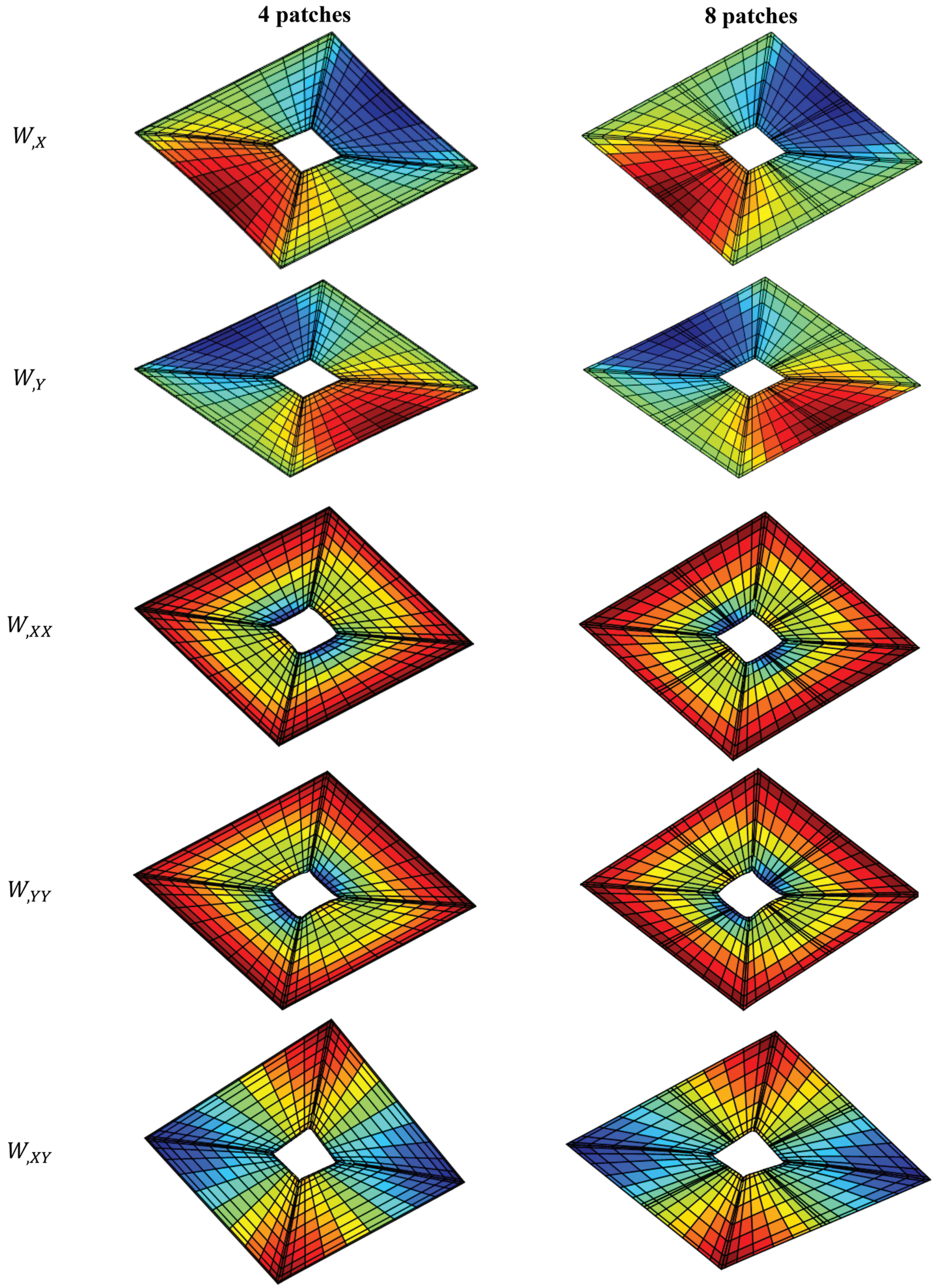

FIGURE 21 Distribution of the second-order derivatives of the deflection for a simply supported square plate with a cutout

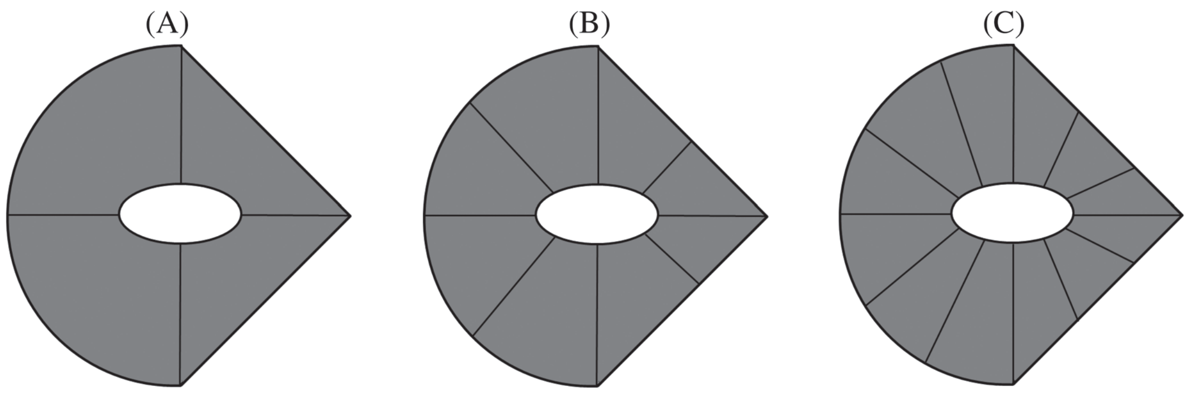

FIGURE 22 Three patch patterns for an irregular plate: (A) Four patches (B) eight patches (C) twelve patches

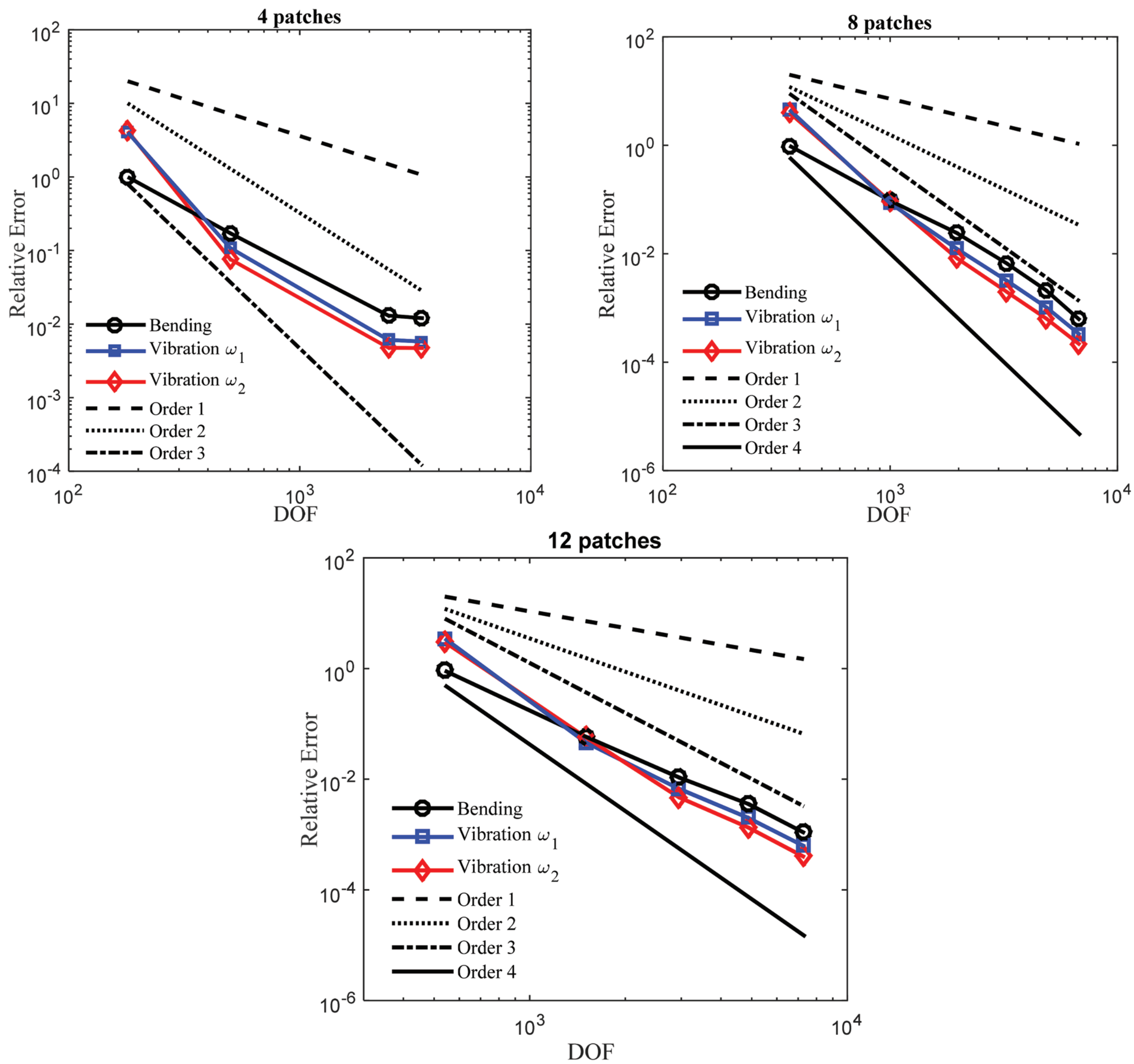

FIGURE 23 Convergence results for bending and vibration analysis of a clamped irregular plate

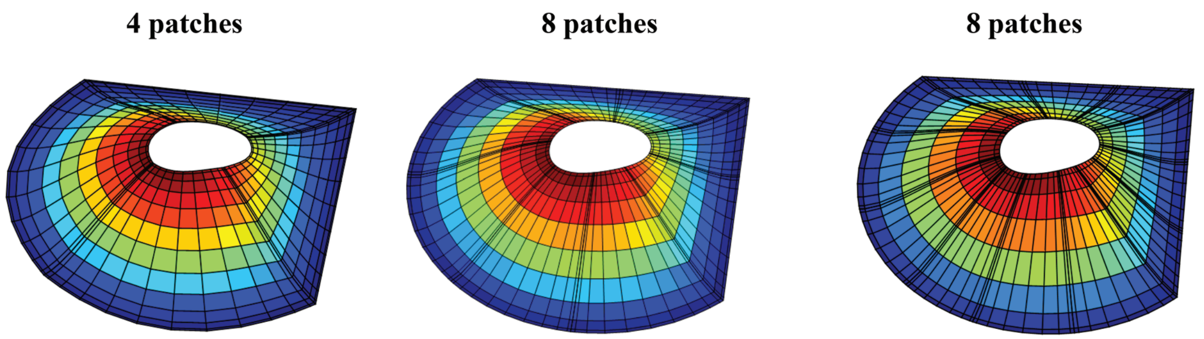

FIGURE 24 Distribution of deflection for a clamped irregular plate

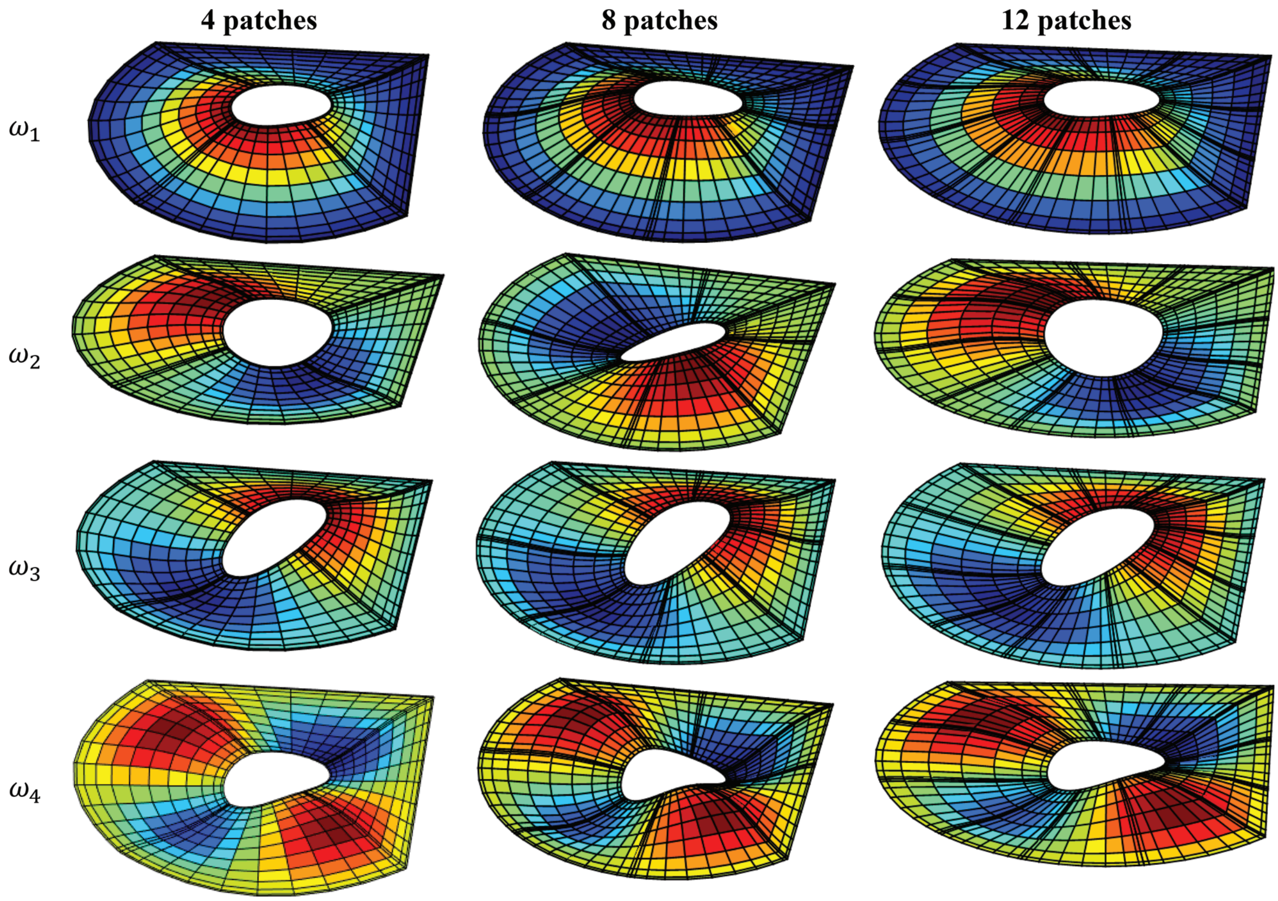

FIGURE 25 The first four vibrational mode shapes for a clamped irregular plate

TABLE 5 Convergence of the non-dimensional maximum deflection for a clamped irregular plate

	Clamped		
$n = m$	4 patches	8 patches	12 patches
5	0.701	0.766	0.796
7	0.821	0.826	0.837
9	0.833	0.84	0.843
11	0.835	0.844	0.845
13	0.836	0.845	0.846
15	0.836	0.846	0.846

TABLE 6 Convergence of the non-dimensional natural frequencies for a clamped irregular plate

		Clamped		
	$n = m$	4 patches	8 patches	12 patches
$\overline{\omega}_1$	5	4.608	4.514	4.352
	7	4.218	4.212	4.188
	9	4.188	4.172	4.168
	11	4.184	4.164	4.162
	13	4.184	4.160	4.160
	15	4.182	4.160	4.160
$\overline{\omega}_2$	5	6.438	6.536	6.326
	7	6.02	6.034	6.012
	9	6.012	5.996	5.992
	11	6.012	5.988	5.986
	13	6.012	5.984	5.984
	15	6.012	5.984	5.982
$\overline{\omega}_3$	5	7.576	7.406	7.268
	7	7.168	7.148	7.130
	9	7.136	7.118	7.114
	11	7.128	7.110	7.110
	13	7.128	7.108	7.106
	15	7.126	7.106	7.106
$\overline{\omega}_4$	5	9.094	9.166	8.904
	7	8.622	8.640	8.604
	9	8.592	8.568	8.562
	11	8.588	8.552	8.550
	13	8.586	8.548	8.546
	15	8.586	8.546	8.546

natural frequencies for different patch patterns and grids. Quite rapid convergence trend is found, and fairly accurate results can be obtained even with fairly coarse grids, for example, $n = m = 9$. Figures 24 and 25 display the distributions of deflections and mode shapes. The consistency of the results for different patch patterns expresses the efficiency of the method for irregular domains.

5 | CONCLUSION

A novel numerical solution method, called the multi-patch VDQ method, was developed in this article to solve the bending and vibration problems of the shear deformation plate theory within strain gradient elasticity. The matrix form of the formulation was derived by following the shear deformation plate model and Mindlin's strain gradient elasticity theory. The solution domain of the plate problem was divided into sub-domains called patches and the VDQ method in conjunction with a FE mapping procedure was applied to discretize the energy functional within each patch. To satisfy the C^1-continuity requirement stemming from the variational formulation, the corresponding compatibility conditions for the primary problem variables and their derivatives were applied through the interfaces of the adjacent patches. The Lagrange multiplier technique and the penalty method were employed to impose the compatibility and boundary conditions, respectively. The plate problem was solved for linear static bending and vibration with different solution domains to demonstrate the applicability and efficiency of the method for both regular and irregular plate domains.

The convergence studies revealed that accurate results can be obtained by either increasing the number of grid points or the number of patches, while very few patches or curved domains lead to the least accurate results. The accuracy of the proposed method was also assessed and confirmed by comparisons to FE results obtained by higher-order elements. The fulfillment of the required continuity conditions was demonstrated by the proper derivative distributions of deflection.

ORCID

Jalal Torabi https://orcid.org/0000-0001-7525-8442
Jarkko Niiranen https://orcid.org/0000-0002-8898-2576
Reza Ansari https://orcid.org/0000-0002-6810-6624

REFERENCES

1. Shu C. *Differential Quadrature and Its Application in Engineering*. Springer Science & Business Media; 2012.
2. Shu C, Du H. Implementation of clamped and simply supported boundary conditions in the GDQ free vibration analysis of beams and plates. *Int J Solids Struct*. 1997;34(7):819-835.
3. Shu C, Chen W, Xue H, Du H. Numerical study of grid distribution effect on accuracy of DQ analysis of beams and plates by error estimation of derivative approximation. *Int J Numer Methods Eng*. 2001;51(2):159-179.
4. Hua L, Lam KY. The generalized differential quadrature method for frequency analysis of a rotating conical shell with initial pressure. *Int J Numer Methods Eng*. 2000;48(12):1703-1722.
5. Karami G, Malekzadeh P. Application of a new differential quadrature methodology for free vibration analysis of plates. *Int J Numer Methods Eng*. 2003;56(6):847-868.
6. Ferreira AJM, Viola E, Tornabene F, Fantuzzi N, Zenkour AM. Analysis of sandwich plates by generalized differential quadrature method. *Math Probl Eng*. 2013;2013:964367.
7. Ansari R, Gholami R, Shojaei MF, Mohammadi V, Sahmani S. Size-dependent bending, buckling and free vibration of functionally graded Timoshenko microbeams based on the most general strain gradient theory. *Compos Struct*. 2013;100:385-397.
8. Torabi J, Ansari R. Thermal buckling of carbon nanocones based on the nonlocal shell model. *Iran J Sci Technol Trans Mech Eng*. 2019;43(1):723-732.
9. Shojaei MF, Ansari R. Variational differential quadrature: a technique to simplify numerical analysis of structures. *App Math Model*. 2017;49:705-738.
10. Ansari R, Torabi J, Shojaei MF. Buckling and vibration analysis of embedded functionally graded carbon nanotube-reinforced composite annular sector plates under thermal loading. *Compos B Eng*. 2017;109:197-213.
11. Ansari R, Shojaei MF, Gholami R. Size-dependent nonlinear mechanical behavior of third-order shear deformable functionally graded microbeams using the variational differential quadrature method. *Compos Struct*. 2016;136:669-683.
12. Ansari R, Torabi J. Numerical study on the free vibration of carbon nanocones resting on elastic foundation using nonlocal shell model. *Appl Phys A*. 2016;122(12):1-13.
13. Ansari R, Hasrati E, Torabi J. Effect of external pressure on the vibration analysis of higher order shear deformable FG-CNTRC spherical panels. *Eng Comput*. 2020;1-1312. https://doi.org/10.1007/s00366-020-01138-0
14. Karami G, Malekzadeh P. Static and stability analyses of arbitrary straight-sided quadrilateral thin plates by DQM. *Int J Solids Struct*. 2002;39(19):4927-4947.
15. Shojaee M, Setoodeh AR, Malekzadeh P. Vibration of functionally graded CNTs-reinforced skewed cylindrical panels using a transformed differential quadrature method. *Acta Mech*. 2017;228(7):2691-2711.
16. Torabi J, Ansari R, Hassani R. Numerical study on the thermal buckling analysis of CNT-reinforced composite plates with different shapes based on the higher-order shear deformation theory. *Eur J Mech A/Solids*. 2019;73:144-160.
17. Akgün G, Kurtaran H. Large displacement transient analysis of FGM super-elliptic shells using GDQ method. *Thin-Walled Struct*. 2019;141:133-152.
18. Zhang B, Li H, Kong L, Zhang X, Feng Z. Strain gradient differential quadrature finite element for moderately thick micro-plates. *Int J Numer Methods Eng*. 2020;121(24):5600-5646.
19. Chen CN. A generalized differential quadrature element method. *Comput Methods Appl Mech Eng*. 2000;188(1–3):553-566.
20. Fantuzzi N. *Generalized Differential Quadrature Finite Element Method Applied to Advanced Structural Mechanics*. Ph.D. thesis. University of Bologna, Bologna, Italy; 2013.
21. Viola E, Tornabene F, Fantuzzi N. Generalized differential quadrature finite element method for cracked composite structures of arbitrary shape. *Compos Struct*. 2013;106:815-834.
22. Fantuzzi N, Tornabene F, Viola E. Generalized differential quadrature finite element method for vibration analysis of arbitrarily shaped membranes. *Int J Mech Sci*. 2014;79:216-251.
23. Liu B, Ferreira AJM, Xing YF, Neves AMA. Analysis of composite plates using a layerwise theory and a differential quadrature finite element method. *Compos Struct*. 2016;156:393-398.

24. Ansari R, Torabi J, Hassani R. Vibration analysis of FG-CNTRC plates with an arbitrarily shaped cutout based on the variational differential quadrature finite element method. *Mater Res Exp*. 2019;6(12):125086.
25. Ansari R, Hassani R, Torabi J. Mixed-type formulation of higher-order shear deformation theory for vibration and buckling analysis of FG-GPLRC plates using VDQFEM. *Compos Struct*. 2020;235:111738.
26. Ansari R, Hassani R, Hasrati E, Rouhi H. Geometrically nonlinear vibrations of FG-GPLRC cylindrical panels with cutout based on HSDT and mixed formulation: a novel variational approach. *Acta Mech*. 2021;232:3417-3439. https://doi.org/10.1007/s00707-021-03000-w
27. Mindlin RD. Micro-structure in linear elasticity. *Arch Rational Mech Anal*. 1964;16(1):51-78.
28. Mindlin RD. Second gradient of strain and surface-tension in linear elasticity. *Int J Solids Struct*. 1965;1(4):417-438.
29. Lam DC, Yang F, Chong ACM, Wang J, Tong P. Experiments and theory in strain gradient elasticity. *J Mech Phys Solids*. 2003;51(8):1477-1508.
30. Karlis GF, Charalambopoulos A, Polyzos D. An advanced boundary element method for solving 2D and 3D static problems in Mindlin's strain-gradient theory of elasticity. *Int J Numer Methods Eng*. 2010;83(11):1407-1427.
31. Ghayesh MH, Amabili M, Farokhi H. Nonlinear forced vibrations of a microbeam based on the strain gradient elasticity theory. *Int J Eng Sci*. 2013;63:52-60.
32. Khakalo S, Niiranen J. Form II of Mindlin's second strain gradient theory of elasticity with a simplification: for materials and structures from nano-to macro-scales. *Eur J Mech A/Solids*. 2018;71:292-319.
33. Solyaev YO, Lurie SA. Trefftz collocation method for two-dimensional strain gradient elasticity. *Int J Numer Methods Eng*. 2021;122(3):823-839.
34. Auffray N, Bouchet R, Brechet Y. Strain gradient elastic homogenization of bidimensional cellular media. *Int J Solids Struct*. 2010;47(13):1698-1710.
35. Romanoff J, Reddy JN. Experimental validation of the modified couple stress Timoshenko beam theory for web-core sandwich panels. *Compos Struct*. 2014;111:130-137.
36. Khakalo S, Balobanov V, Niiranen J. Modelling size-dependent bending, buckling and vibrations of 2D triangular lattices by strain gradient elasticity models: applications to sandwich beams and auxetics. *Int J Eng Sci*. 2018;127:33-52.
37. Khakalo S, Niiranen J. Anisotropic strain gradient thermoelasticity for cellular structures: plate models, homogenization and isogeometric analysis. *J Mech Phys Solids*. 2020;134:103728.
38. Torabi J, Niiranen J. Microarchitecture-dependent nonlinear bending analysis for cellular plates with prismatic corrugated cores via an anisotropic strain gradient plate theory of first-order shear deformation. *Eng Struct*. 2021;236:112117.
39. Papanicolopulos SA, Zervos A, Vardoulakis I. A three-dimensional C^1 finite element for gradient elasticity. *Int J Numer Methods Eng*. 2009;77(10):1396-1415.
40. Zhao J, Chen WJ, Lo SH. A refined nonconforming quadrilateral element for couple stress/strain gradient elasticity. *Int J Numer Methods Eng*. 2011;85(3):269-288.
41. Torabi J, Ansari R, Darvizeh M. A C1 continuous hexahedral element for nonlinear vibration analysis of nano-plates with circular cutout based on 3D strain gradient theory. *Compos Struct*. 2018;205:69-85.
42. Sze KY, Yuan WC, Zhou YX. Four-node tetrahedral elements for gradient-elasticity analysis. *Int J Numer Methods Eng*. 2020;121(16):3660-3679.
43. Torabi J, Niiranen J, Ansari R. Nonlinear finite element analysis within strain gradient elasticity: Reissner-Mindlin plate theory versus three-dimensional theory. *Eur J Mech A/Solids*. 2021;87:104221.
44. Fischer P, Klassen M, Mergheim J, Steinmann P, Müller R. Isogeometric analysis of 2D gradient elasticity. *Comput Mech*. 2011;47(3):325-334.
45. Niiranen J, Khakalo S, Balobanov V, Niemi AH. Variational formulation and isogeometric analysis for fourth-order boundary value problems of gradient-elastic bar and plane strain/stress problems. *Comput Methods Appl Mech Eng*. 2016;308:182-211.
46. Niiranen J, Kiendl J, Niemi AH, Reali A. Isogeometric analysis for sixth-order boundary value problems of gradient-elastic Kirchhoff plates. *Comput Methods Appl Mech Eng*. 2017;316:328-348.
47. Thai S, Thai HT, Vo TP, Patel VI. Size-dependant behaviour of functionally graded microplates based on the modified strain gradient elasticity theory and isogeometric analysis. *Comput Struct*. 2017;190:219-241.
48. Balobanov V, Niiranen J. Locking-free variational formulations and isogeometric analysis for the Timoshenko beam models of strain gradient and classical elasticity. *Comput Methods Appl Mech Eng*. 2018;339:137-159.
49. Dittmann M, Schuß S, Wohlmuth B, Hesch C. Weak Cn coupling for multipatch isogeometric analysis in solid mechanics. *Int J Numer Methods Eng*. 2019;118(11):678-699.

How to cite this article: Torabi J, Niiranen J, Ansari R. Multi-patch variational differential quadrature method for shear-deformable strain gradient plates. *Int J Numer Methods Eng*. 2022;123(10):2309-2337. doi: 10.1002/nme.6939